SANDIA REPORT

SAND2000-0919
Unlimited Release
Printed April 2000

Characterization of Si Nanostructures Using Internal Quantum Efficiency Measurements

Saleem H. Zaidi

Prepared by
Sandia National Laboratories
Albuquerque, New Mexico 87185 and Livermore, California 94550

Sandia is a multiprogram laboratory operated by Sandia Corporation, a Lockheed Martin Company, for the United States Department of Energy under Contract DE-AC04-94AL85000.

Sandia National Laboratories

Issued by Sandia National Laboratories, operated for the United States Department of Energy by Sandia Corporation.

Available to DOE and DOE contractors from
Office of Scientific and Technical Information
P.O. Box 62
Oak Ridge, TN 37831

Prices available from (703) 605-6000
Web site: http://www.ntis.gov/ordering.htm

Available to the public from
National Technical Information Service
U.S. Department of Commerce
5285 Port Royal Rd
Springfield, VA 22161

DISCLAIMER

Portions of this document may be illegible in electronic image products. Images are produced from the best available original document.

SAND2000-0919
Unlimited Release
Printed April 2000

CHARACTERIZATION OF Si NANOSTRUCTURES USING INTERNAL QUANTUM EFFICIENCY MEASUREMENTS

Saleem H. Zaidi
Gratings, Incorporated
7104 Jefferson, NE
Albuquerque, NM 87109

Sandia Contract # BE-8229

ABSTRACT

Hemispherical reflectance and internal quantum efficiency measurements have been employed to evaluate the response of Si nanostructured surfaces formed by using random and periodic reactive ion etching techniques. Random RIE-textured surfaces have demonstrated solar weighted reflectance of ≈ 3 % over 300-1200-nm spectral range even without the benefit of anti-reflection films. Random RIE-texturing has been found to be applicable over large areas (~180 cm^2) of both single and multicrystalline Si surfaces. Due to the surface contamination and plasma-induced damage, RIE-textured surfaces did not initially provide increased short circuit current as expected from the enhanced absorption. Improved processing combined with wet-chemical damage removal etches resulted in significant improvement in the short circuit current with IQEs comparable to the random, wet-chemically textured surfaces. An interesting feature of the RIE-textured surfaces was their superior performance in the near IR spectral range.

The response of RIE-textured periodic surfaces can be broadly classified into three distinct regimes. One-dimensional grating structures with triangular profiles are characterized by exceptionally low, polarization-independent reflective behavior. The reflectance response of such surfaces is similar to a graded-index anti-reflection film. The IQE response from these surfaces is severely degraded in the UV-Visible spectral region due to plasma-induced surface damage. One-dimensional grating structures with rectangular profiles exhibit spectrally selective absorptive behavior with somewhat similar IQE response. The third type of grating structure combines broadband anti-reflection behavior with significant IQE enhancement in 800-1200-nm spectral region. The hemispherical reflectance of these 2D grating structures is comparable to random RIE-textured surfaces. The IQE enhancement in the long wavelength spectral region can be attributed to increased coupling into obliquely propagating transmitted diffracted orders inside the Si substrate.

Random RIE texturing techniques are expected to find widespread commercial applicability in low-cost, large-area multicrystalline Si solar cells. Grating-texturing techniques are expected to find applications in thin-film and space solar cells.

Table of Contents

1. Introduction 3

2. Part I. Reactive Ion Etching for Random Nanoscale Texturing of Si 4

2a. Surface Texturing with RIE 4

2b. Spectral Reflectance Measurements of Random RIE-Textured Surfaces 5

2c. Solar Cell Fabrication on Random RIE-Textured Surfaces 8

2d. Internal Quantum Efficiency Measurements 8

2e. IQE Improvement with RCA Clean 8

2f. IQE Improvement with Surface Treatments 10

2g. IQE Enhancement in IR Region: Structural Dependence 13

2h. Discussion of Results and Future Work 15

3. Part II. Periodic Surface Texturing of Si 17

3a. Sub-wavelength Periodic Structures for Solar Cell Applications 17

3b. Etching of Periodic Structures in Si 18

3c. Hemispherical Reflectance Measurements 18

3d. Internal Quantum Efficiency Measurements of Grating Solar Cells 22

3e. Diffractive Approach for Solar Cells 24

3f. Discussion of Results 26

4. Summary 30

5. References 31

1. Introduction

The performance of a solar cell is a critical function of its internal quantum efficiency (IQE), which determines the relative percentage of photo-generated electron-hole pairs (EHPs) lost to recombination after accounting for reflection losses [1]. Therefore, in solar cell research aimed at improved efficiency, the primary goal is enhancement of light absorption while minimizing recombination losses. Figure 1 shows Si surface reflectance and absorption depth as a function of wavelength. It is seen that Si reflectance is high ~ 52 % in the UV, and reduces to ~ 33 % in most of the visible to near IR range. The spectral absorption curve shows that most

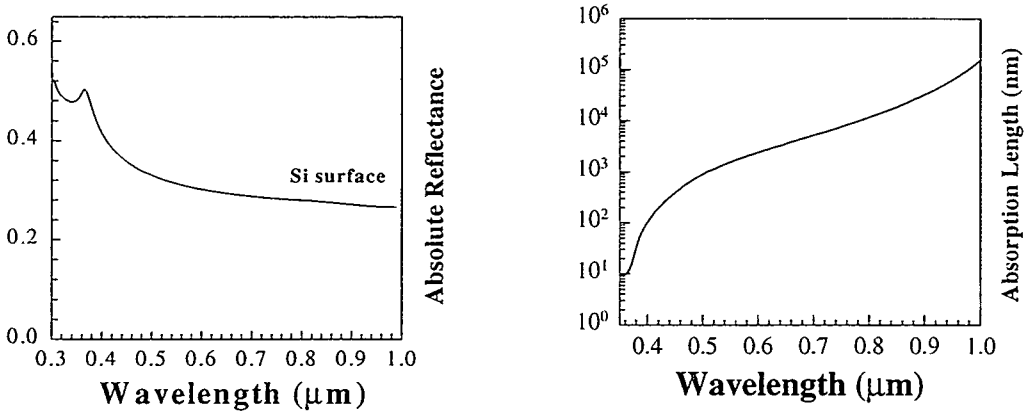

Figure 1. Spectral reflectance (left) and absorption depth in Si (right).

of the UV-Visible (0.3~ 0.6 μm) light is absorbed to within ~ 1 μm of the top surface. At longer wavelengths, particularly near the band edge, the absorption is much weaker, i.e., absorption depth of ~ 100 μm at 1-μm wavelength. In most of the terrestrial and space solar cells, the top surface p-n junction formed within ~ 0.1-0.5 μm of the surface collects almost 100 % of the photo-generated EHPs in the UV-Visible spectral range. In near IR range, however, a fraction of EHPs is lost to bulk recombination. Ideally, optimum cell performance is achieved for cell thickness a fraction of the minority carrier diffusion length [2]. Reduced Si thickness is also attractive for lower bulk recombination losses, and relaxed material quality requirements. In order to improve near IR absorption in conventional and thin-film Si solar cells, light trapping schemes based on geometrical optics considerations have been developed [3]. The trapping scheme takes advantage of the fact that due to high refractive index n of Si, the light inside Si propagating outside a narrow angular cone defined by the critical angle $\theta_c = Sin^{-1}(1/n)$ is subjected to total internal reflection. Therefore, by re-directing light inside Si at oblique angles ($>\theta_c$), total internal reflection causes multiple bounces within the cell enhancing its absorption probability [4]. Yablonovitch in a detailed statistical analysis has shown that in comparison with a planar sheet, the effective absorption can be enhanced by as much as a factor of $4n^2$ [5]. However, in order to reach this statistical limit, surface texture must fully randomize incident light. Deckman, et al., [6] have shown that optimal texture dimensions needed to achieve this statistical randomization are comparable to light wavelengths inside Si. For Si in the UV-near IR spectral range, this translates to feature sizes in 50-300 nm range. When optical wavelengths are comparable, or larger than surface features, geometrical optics considerations do not provide a clear picture. Instead an accurate vector modeling of light interaction is required [7]. The enhanced absorption in sub-wavelength structures, particularly in the UV-Visible spectral range is based on the waveguide resonances in $\lambda/2n$ type cavities [8].

This report, divided into parts I & II, examines the performance of sub-wavelength random and periodic surfaces integrated into conventional solar cell devices. Part I evaluates the performance of randomly etched surfaces, and part II evaluates structure performance of uniformly textured surfaces.

2. Part I. Reactive Ion Etching for Random Nanoscale Texturing of Si

2a. Surface Texturing with RIE

Surface texturing aimed at enhanced absorption in Si has been extensively investigated by geometrical optics. Geometrical textures reduce reflection and improve absorption in IR region by oblique coupling of light into the semiconductor. Despite their effectiveness and industrial applications, geometrical texturing schemes suffer from several disadvantages that limit their effectiveness. Some of these are listed below.

a) Wet-chemical anisotropic etching used to form random pyramids in (100) crystal orientation is not effective in texturing of low-cost multi-crystalline wafers,
b) Anti-reflection films coated on random features aimed at reflection reduction have a resonant structure, which limits their effectiveness to a narrow range of angles and wavelengths, and
c) Reduced IR absorption in thin-film (< 10 μm) Si solar cells.

A low-cost, large area, random, maskless texturing scheme independent of crystal orientation is expected to significantly impact terrestrial photovoltaic technology, particularly in the area of mc-Si solar cells.

Reactive ion etching (RIE) techniques in Si have been extensively developed over the last two decades as part of integrated circuit manufacturing base. These RIE techniques have been adapted for fabrication of sub-wavelength textures in both single and mc-Si. First such textures were reported by Gittleman, et al., [9]. They developed a reactive sputter etching process in Cl_2 plasma using Si wafers coated with 100-nm thick Al film on their backside. The textured surface appeared velvet black to the naked eye, and consisted of randomly spaced columns with diameters and spaces varying between 100 and 300 nm at depths varying from ~ 0-2000 nm. Craighead et al., [10] reported on a similar texturing scheme in a gas mixture consisting of CCl_2F_2, Ar, and O_2 plasma. The texture process was aided by placing Al samples (~ 2 cm^2) on the quartz cathode close to the Si samples. The textured features consisted of randomly etched columns with diameters varying between 50-100 nm at depths of ~ 1000 nm. For both of these textures, reflectance was measured to be essentially zero below λ ~ 1000 nm. Criaghead et al., [11] also reported on two methods for fabrication of black Si surfaces: a) deposition of a thin island film to act as an etch mask for anisotropic reactive ion etching, and b) an in-situ deposition of an Al-film mask for RIE [12]. More recently, Jansen, et al., have reported on a black Si method using a low-temperature RIE process in $SF_6/CHF_3/O_2$ plasma [13]. The texture consisted of very high aspect ratio, randomly etched Si columns with diameters of ~ 1000 nm and depths of ~ 30000 nm. These textures exhibit low reflectance, but are not expected to be suitable for solar cells due to their high aspect ratios. RIE of large area (10x 10 cm^2) mc-Si has been reported by Burger, et al. [14]. No processing details were reported, except that the RIE process was uniform only to a diameter of ~ 8 cm, leaving outer ~ 2-cm wide edges without any texture. Finally, Inomata, et al., have reported on solar cells fabricated on 15x15 cm^2 mc-Si solar cells using Cl_2 plasma with an energy conversion efficiency of ~ 17 % [15].

From the literature review, it is clear that the random RIE texturing techniques can be effective in reducing surface reflection. We have developed RIE texturing techniques over large areas using SF_6/O_2 plasma chemistry, equally applicable to either single or multi-crystalline Si. The textured surfaces exhibit reflection ~ 1-5 % for wavelengths below 1 μm without the benefit of anti-reflection films. RIE was carried out in a Plasma-Therm 790 reactor. The cathode in the sample chamber consists of Graphite, and chamber walls and anode are made of aluminum. A large parameter space with respect to the power, pressures, gas ratios, flow rates, and etch times was investigated. A narrow parameter space was determined to be useful for texturing Si wafers varying in diameter upto 6" (~180 cm^2), mc-Si wafers of ~ 130 cm^2 have also been similarly textured. Figure 2 shows examples of RIE-textured mc-Si surfaces. The textured regions appear dark brown to black to the naked eye. The texture microstructure was investigated using scanning electron microscope (SEM). Figure 3 shows three types of structures that have been textured using variations in RIE parameters. These results demonstrate that RIE

processes can be employed to texture a wide range of surface profiles, and thus provide some degree of tunability in terms of light interaction with nanostructured surfaces.

An alternative to rie texturing aimed at reduced surface reflection has also been investigated. This scheme is based on electrochemical etching of Si to convert top surface layer into a porous material. Tsuo, et al., [16] have reported on reflection properties of porous Si. However, there are many problems associated with porous Si in solar cell structures. The high resistivity and a lack of understanding of EHP generation and transport mechanisms of porous Si make it difficult to design high efficiency solar cell structures using porous Si layer as the light absorbing medium.

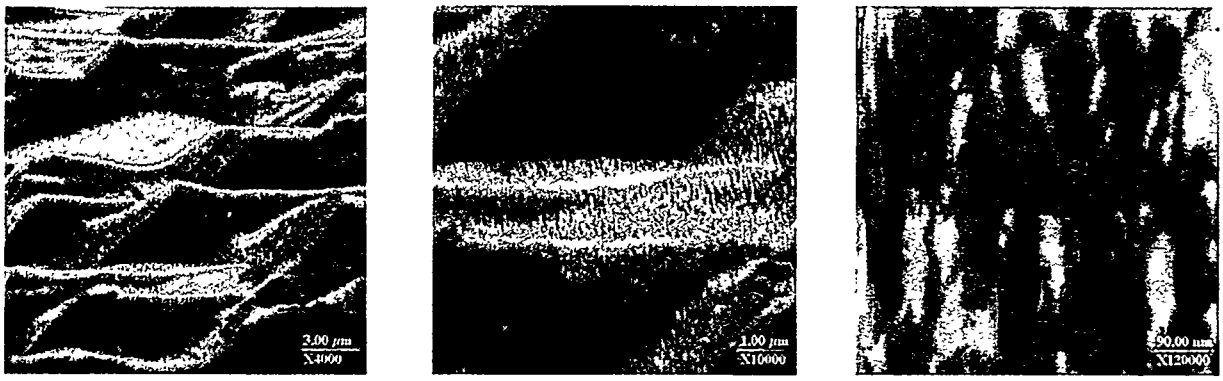

Figure 2. SEM pictures of RIE-textured mc-Si surfaces with increasing magnification from left-to-right.

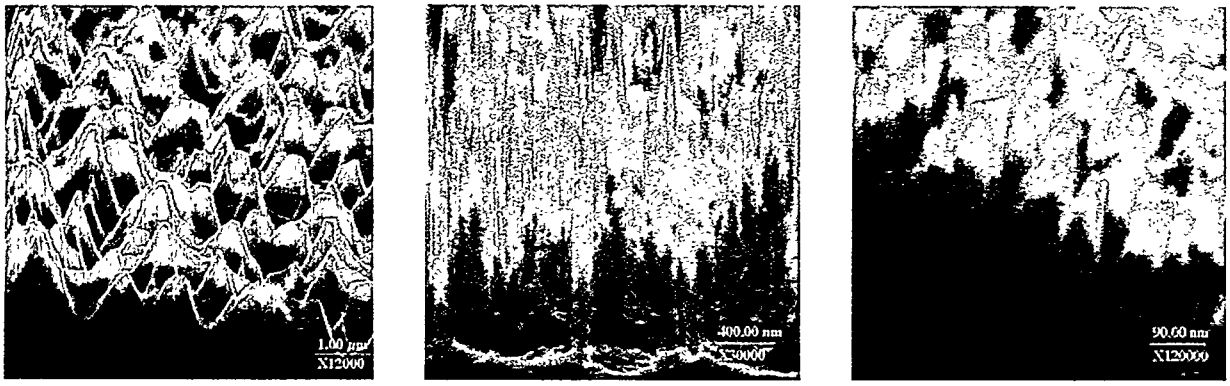

Figure 3. SEM pictures of different types of Si nanostructures formed by RIE process variations, approximate feature linewidths ~ 0.1-0.6 μm large pyramids (left), needles ~ 0.03-0.07 μm (middle), and small pyramids ~ 0.02-0.05 μm (right).

2b. Spectral Reflectance Measurements of Random RIE-Textured Surfaces

Spectral reflectance measurements of textured surfaces were carried out using a Cary Model 5E (UV-VIS-NIR) spectrophotometer and a Labsphere (RSA-CA-50) integrating sphere. This system utilizes a photo-multiplier tube for 300-800 nm spectral range, and a Lead Sulfide detector for 800-1200-nm spectral range. Figure 4 plots the measured hemispherical reflectance measurements from conventional, wet-chemical and RIE textured surfaces shown in Fig. 2 The increase in reflectance in the 1.1-1.2-μm spectral region corresponds to the light reflected from the back surface, and transmitted back into the air. We notice that for the RIE-textured surface, solar-weighted reflectance (SWR) is ~ 3 % over the entire spectral region, for the planar and wet-textured surfaces, SWR values are ~ 43 & 21 % respectively. Figure 5 shows hemispherical reflectance measurements from the

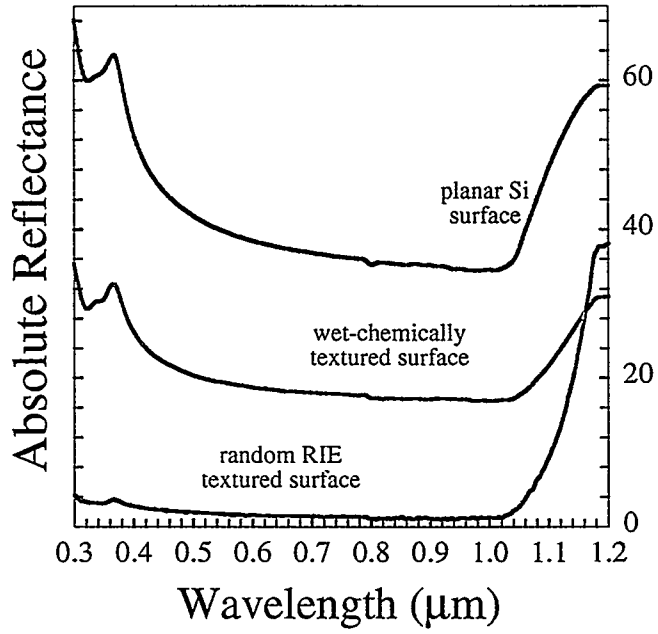

Figure 4. Hemispherical reflectance measurements of the conventional wet-chemical and RIE textured surfaces without anti-reflection films, polished Si reflectance measured under identical conditions is also shown.

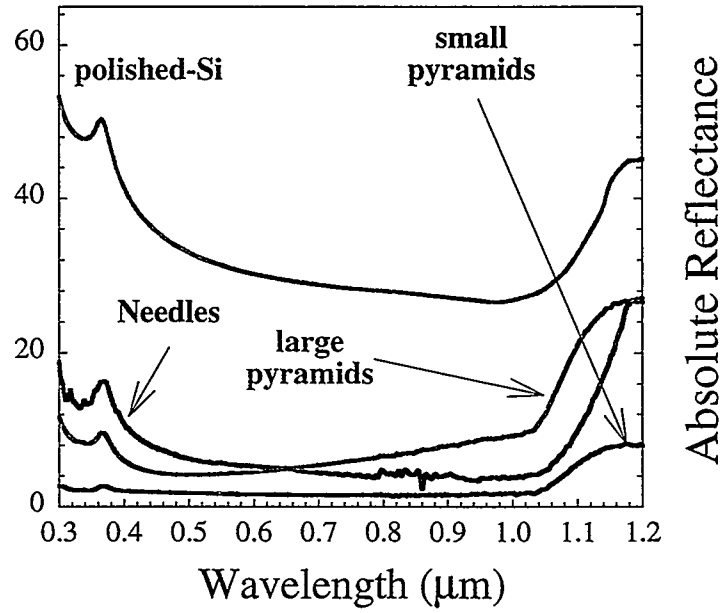

Figure 5. Hemispherical reflectance measurements of the three RIE textures shown in Fig. 3.

three surfaces shown in Fig. 3. The lowest spectral reflection is from the small pyramids, the large pyramids show lower UV and higher IR reflectance in comparison with needle-like features. Using anti-reflection films, surface reflection can be further reduced. Figure 6 shows hemispherical reflectance measurements from the planar, wet and RIE textured (large pyramids in Fig. 3) surfaces after AR coating. It is seen that the SWR has been reduced to ~ 22, 9 & 7 % respectively. Comparison of reflectance measurements of RIE-textured surfaces in Figs. 4-6 shows that significantly lower reflectance is achievable even without the benefit of anti-reflection films.

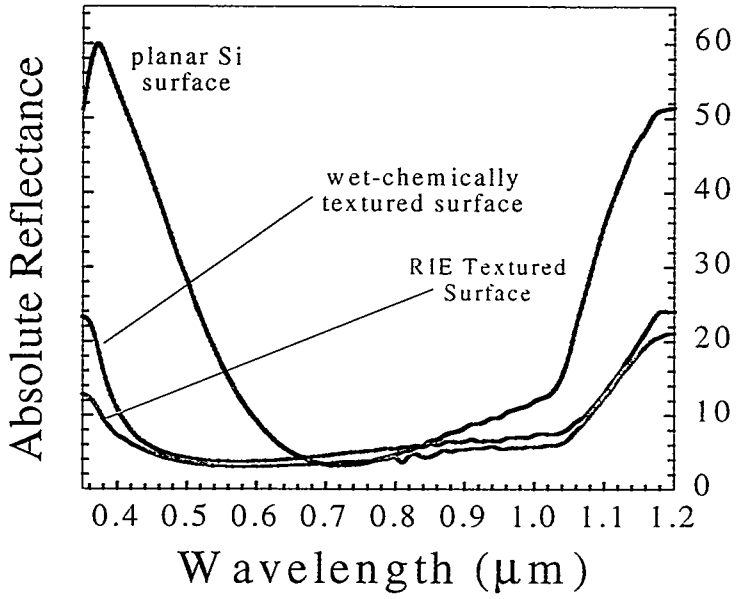

Figure 6. Hemispherical reflectance measurements of planar and textured surfaces coated with anti-reflection silicon-nitride film.

The nanostructures described above combine broadband anti-reflection properties with low-cost fabrication schemes, which are fully compatible with large area requirements of terrestrial photovoltaic industry. In order to incorporate nanostructures into conventional solar cells devices, a number of technical issues have to be addressed. Some of these areas of concern are listed below.

a) RIE process used for texturing Si introduces surface damage [17]. Since nanoscale features have large surface-to-volume ratios, and are strong absorbers of light in the short wavelength region, a significant fraction of EHPs is lost to recombination without adequate surface passivation,
b) Light absorption in nanostructures is a function of both the feature size and profile, so the lowest reflection surfaces may not be ideal for optimized carrier collection across the p-n junction, and
c) The formation of a p-n junction on these nanoscale features may require optimization of the conventional solar cell p-n junctions. For instance, a conformal shallow junction (~ 50-100 nm) may be more appropriate than a deeper junction that lies below the textured region.

The rest of this report describes our technical efforts aimed at solving some of the issues raised above. Experimental results, thus far, demonstrate that with appropriate process optimizations, the RIE-texturing has the potential to be superior to the conventional wet-texturing technology.

2c. Solar Cell Fabrication on Random RIE-Textured Surfaces

Solar cells were fabricated on 4" diameter, p-type, ~ 1 Ω-cm resistivity wafers at the Photovoltaic Device Fabrication Laboratory (PDFL) at Sandia National Laboratories. Wafers were RIE textured and RCA cleaned prior to emitter diffusion. The junction depth was nominally ~ 0.5 μm on planar regions. For IQE comparison between planar and textured regions on the same wafer, a region of ~ 2x2 cm^2 was protected from texturing during RIE. Back surface fields were formed on the rough backside by depositing 1-μm thick Al film, and annealing in O_2 ambient for 30-minutes at 900 °C. This process also results in ~ 10-nm thick passivating oxide film. Front surface contacts were made using a lift-off process with Ti:Pd:Ag (100:100:6000-nm thickness) films. The back surface contacts is made by depositing ~ 1-μm thick Al film on the backside. Metal contacts are annealed in forming gas at 400 °C for 30 minutes. Finally, a 70-nm plasma silicon nitride film is deposited for reducing reflection, and passivating the surface. In order to carry out I-V measurements, cells of area 6x7 cm^2 are cut from the 4" wafer using a CO_2 laser source.

2d. Internal Quantum Measurements

IQE measurements provide an accurate tool for characterization of solar cell performance [1]. In order to assess performance of various textures, it was necessary to compensate for wafer-to-wafer variations in material properties. This can be observed clearly in the IQE measurements of three planar and one wet-chemically textured solar cell shown in Fig. 7 It is seen that cell # 23 has exceptional passivation through the entire spectral region. For this wafer, IR response is similar to the wet-chemically textured region (cell #1). In contrast, cells # 20 & 25 have similar efficiencies in the UV region, but their IR response is significantly less than cells 1 & 23. Since, all these cells were part of the same batch, and were processed identically, and have not been subjected to RIE processes, lack of identical IQEs suggests that there are significant variations in material properties even in the wafers from the same box. In general, for a batch of ~ 21 solar cells was fabricated at a given time, IQEs of the planar regions tended to fall in-between the two extremes shown in Fig. 7. Therefore, in order to have a meaningful assessment of various textures, we measured IQEs from adjacent planar and textured regions of each individual solar cell.

2e. IQE Improvement with the RCA Clean

We have investigated solar cell fabrication on various RIE textured surfaces. The smallest features shown in Fig. 3 (small needles) were consumed during the oxidation and diffusion steps leaving a relatively planar surface, and will not be discussed any further. The larger textures survive the fabrication process, and their IQE responses will be discussed in detail. Figure 8 shows IQE and reflectance responses of two solar cells with slightly different textures. It is seen that for both textures, IQE response in the UV-Visible region is significantly degraded mostly due to RIE-induced surface damage. For texture #1 (Fig. 8, left), the IQE is almost zero at 350 nm, and catches up with the planar region at λ ~ 800 nm. At longer wavelengths, IQE response of this texture is superior to the planar region. For texture # 2 (Fig. 8, right), the UV-visible region response is not as severely reduced as for texture #1, still it is significantly less than that of the planar region. In the long wavelength region, IQE enhancement is not as pronounced as for texture #1. For both of these textures, it is clear that the enhanced absorption is not being translated into electrical current predominantly due to the surface recombination. In addition to surface damage, the performance here may have been further degraded due to the lack of clean surface following the texturing process. RIE texturing introduces a number of metallic impurities can act as recombination centers. In order to remove some of these impurities, we added the RCA clean process following the RIE texturing to solar cell fabrication process. Figure 9 shows IQE measurements for the same two textures shown in Fig. 8. Comparison of texture # 1 in Figs. 8 & 9 shows that the RCA clean has significantly improved the IQE response, although it is still significantly less than the planar surface. Similar comparison of texture # 2

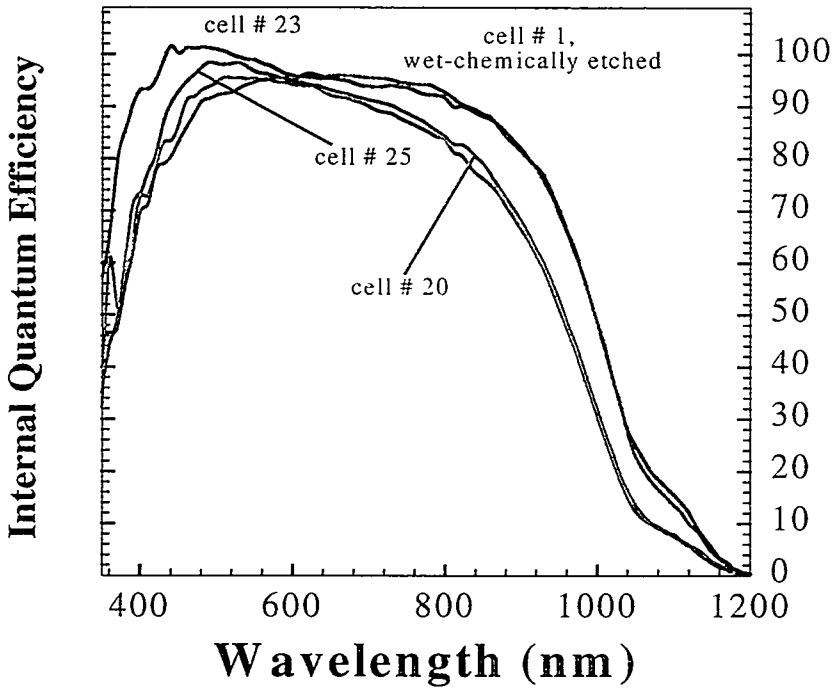

Figure 7. IQE measurements from three planar and one wet-chemically textured solar cells, notice significant variation in near IR efficiencies.

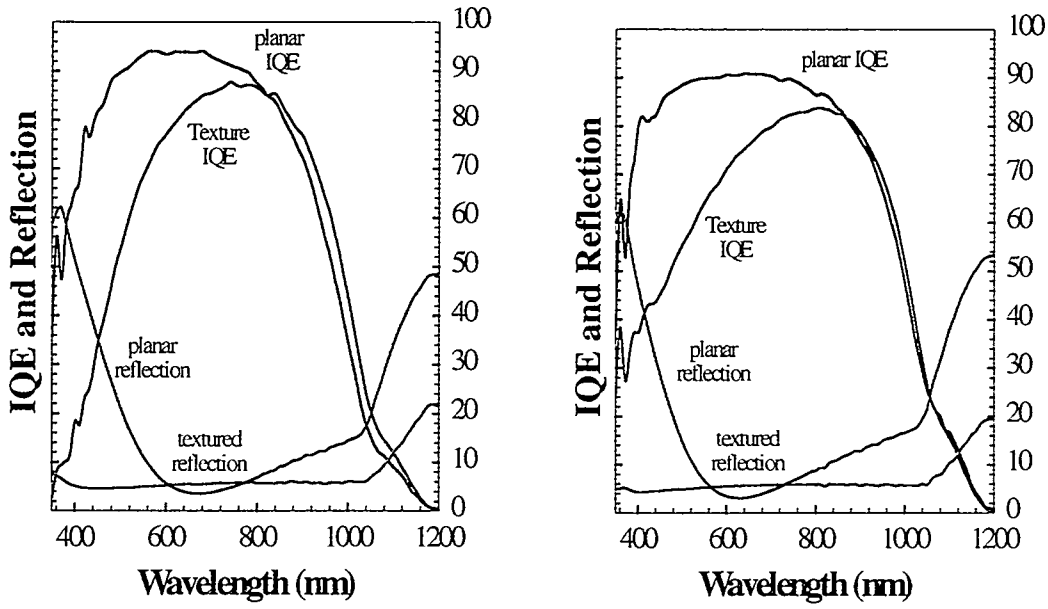

Figure 8. IQE measurements from planar and textured regions of two solar cells, the texturing process on each cell was slightly different.

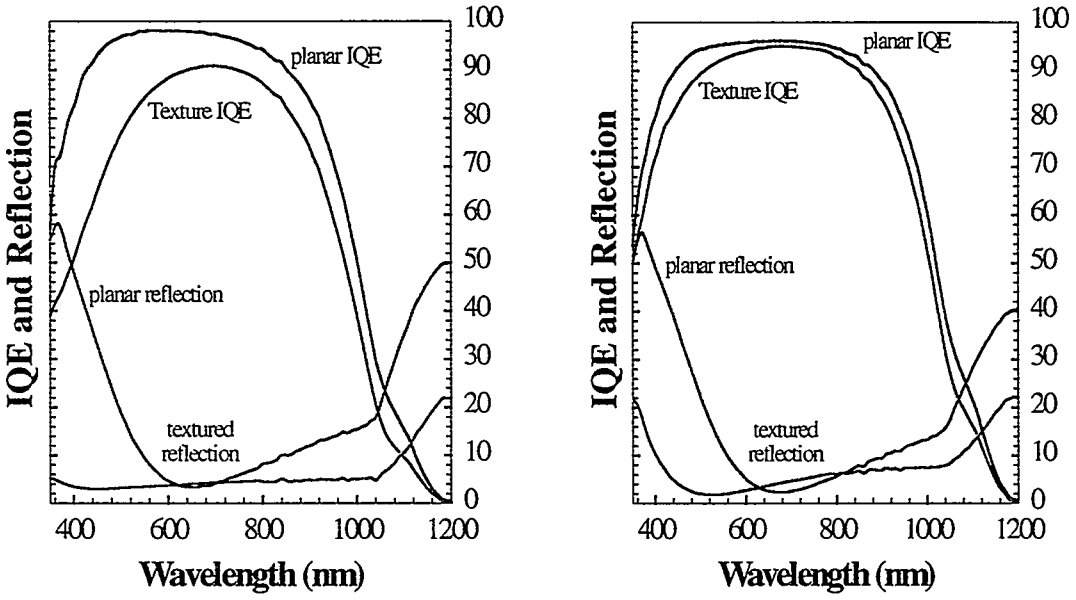

Figure 9. IQE measurements from planar and textured regions of two solar cells, the textured processes on each cell were the same as in Fig. 8, but the cells were fabricated following RCA cleaning process.

shows even more remarkable improvement. Here, the IQE response of the textured region has only slightly been reduced in comparison with the planar surface. These results suggest that in order to match IQEs of the textured and planar regions, RIE-induced surface damage needs to be addressed.

2f. IQE Improvement with Surface Treatments

Despite widespread applicability of RIE processes, it is well known that Si surfaces exposed to plasma processes suffer from surface damage. The nature and severity of this damage is a complex function of many plasma parameters including the chemistry of plasma gases, RF power, dc-bias, temperature and pressure. Various models [18-20] have been proposed to describe the composition of RIE modified surface. These models provide only a qualitative picture, a more accurate analysis requires a precise knowledge of the plasma parameters. In general, Si surfaces exposed to plasma etching consist of a top thin (~ 5 nm) layer consisting entirely of plasma residuals. The layer underneath extending to ~ 10-20 nm consists of heavily damaged Si lattice. The third layer possibly extending from ~ 50 nm to as much as 1000 nm consists of plasma impurities that have diffused into Si during the etching process. The damage caused by RIE processes can degrade the electrical performance of semiconductor devices [17]. In photovoltaic devices, surface damage causes severe degradation of device internal quantum efficiency. Various surface treatments including RTA annealing [21], thermal oxidation and wet-chemical etching [17], and anodic oxidation [22] have been investigated for the recovery of damage-free Si surface from the original RIE-damaged surface. Pang, et al., [17] evaluated various surface treatments including annealing, oxidation, and isotropic wet-chemical etching, and demonstrated that the most effective means of recovering damage-free Si surface was isotropic wet-chemical etching of ~ 50-nm of the top surface. In our work, we have investigated annealing and oxidation without any significant improvements. Wet-chemical etching appeared to be best suited for the recovery process, and agrees well with work reported in Ref [17].

We have investigated damage removal etching (DRE) with KOH and nitric acid solutions. Anisotropic, wet-chemical etching of Si with KOH is well-understood [23]. We used a 40 % KOH solution for removing the surface damage induced by RIE texturing. Figure 10 shows IQE measurements from three solar cells

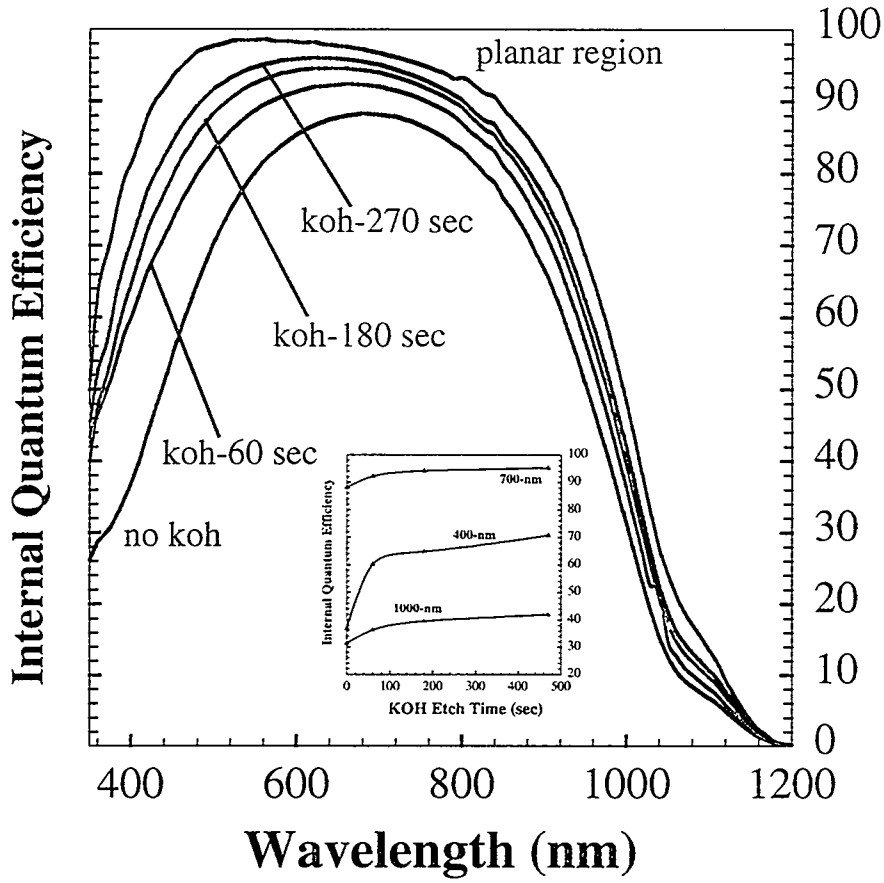

Figure 10. IQE measurements from planar and textured regions of four solar cells as a function of KOH etch time, the RIE- texturing process was the same on each cell.

subjected to varying KOH damage removal etches, for comparison the IQE responses of planar, and RIE-textured surfaces (without DRE) are also shown. It is seen that there is a continuous IQE improvement as a function of KOH time. The inset in this graph plots IQE as a function of KOH-etch time at three different wavelengths. For a planar surface, KOH etch rate is ~ 0.025 μm/min, which suggests that for the maximum etching time of 270 seconds, approximately ~ 0.11-μm thick Si has been removed. It is seen that IQE response in short wavelength region increases sharply following a 60-sec KOH etch. This suggests KOH etch has removed the first and second RIE-damaged layers, which is in good qualitative agreement with the surface damage models discussed earlier. Longer etch times result in much slower IQE improvement, thus suggesting that surface damage may extend much deeper inside Si. Also, notice that KOH DRE improves IQE response over the entire spectral region, even though at longer wavelengths, the absorption depth is much longer than the depth of the damaged layer, thus, indicating the critical role played by the surface passivation.

We have also investigated the recovery of damage-free Si with isotropic nitric acid etch (HNO_3:HF:H_2O in 10:1:4 by volume). Figure 11 shows the IQE measurements for nitric etch times of 5, 10, and 15 seconds. We notice that in comparison with KOH etch, IQE response with nitric acid treatment is somewhat similar for the

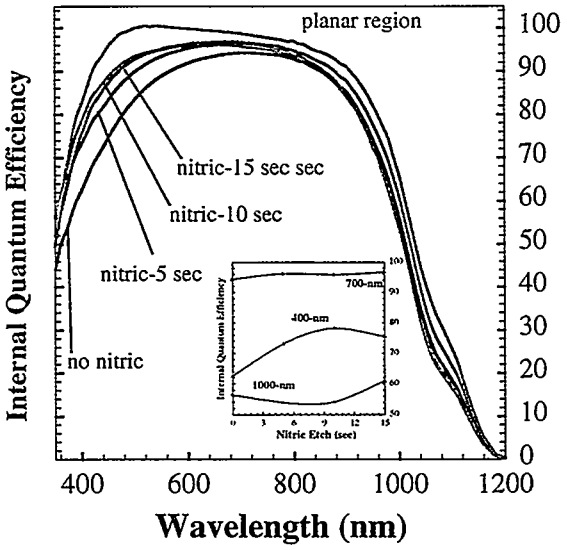

Figure 11. IQE measurements from planar and textured regions of four solar cells as a function of nitric acid etch time, the RIE- texturing process was the same on each cell.

400-nm wavelength. For longer wavelengths, the IQE response does not vary significantly with etch time. For both nitric and KOH etch removal treatments, recovery of damage free surface does not come at the cost of excessive reflection losses. This is observed in the hemispherical reflectance measurements of the KOH-etched surfaces shown in Fig. 12. We notice that as etch time is increased, the UV reflectance increases sharply, however, the long wavelength reflection increase is much lower. This is probably due to the removal of fine textures (~ 20-100 nm), which act as strong absorbers of the short wavelength light. Similar behavior is seen from the nitric acid DRE treatments.

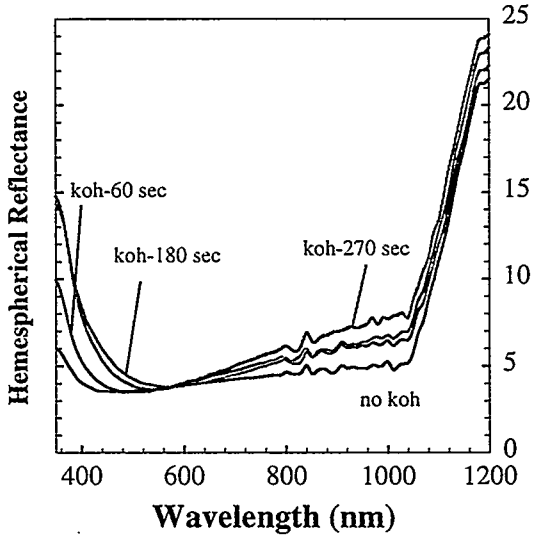

Figure 12. Hemispherical reflectance variation of the textured surfaces of four solar cells as a function of KOH-etching.

In summary, these IQE measurements demonstrate that the RIE-induced surface damage can be removed by appropriate wet-chemical DRE treatments without significant increase in surface reflection.

2g. IQE Enhancement in IR Region: Structural Dependence

In conventional wet-chemically etched surfaces, enhancement in near IR IQE relative to a planar surface is achieved by redirecting incident light inside Si close to the surface. For feature sizes much larger than incident wavelengths, this is achieved by total internal reflection within pyramidal surfaces. We have also observed near IR IQE enhancement with textured features that are either comparable, or smaller than optical wavelengths. This enhancement can best be understood by diffraction mechanisms. A random surface is represented by a series of grating structures with a wide range of frequencies and profiles. If, for instance, the average spacing of these random features is ~ 0.3-0.5 μm [7], the transmitted diffraction orders inside Si propagate at oblique angles. The electron-hole pairs thus generated are much closer to the surface junction than for normally propagating light rays, and therefore, have a higher probability of collection by the junction. In this way, nanoscale textured surface can potentially improve near IR IQE response in comparison with a planar surface. Figures 13-15 show three examples of such behavior. The IQE and EQE ratios in Figs. 13-15 represent measurements from adjacent planar and textured regions of the same cell. For the solar cell in Fig. 13, IQE has been improved in 800-1200-nm spectral region with a peak enhancement by a factor of 1.8 at ~ 1100 nm. The lower IQE response in the short wavelength region is due to the surface damage, since this cell was not subjected to the damage removal wet-chemical etch treatment. For the cell in Fig. 14, a 30-sec KOH damage removal was performed, and was not nearly enough to improve short wavelength IQE response. Peak IQE enhancement by a factor of ~ 1.8 was observed at ~ 1000 nm. For the cell in Fig. 15, a 10-sec nitric acid damage removal etch was performed. Short wavelength IQE shows some improvement, but is still significantly less than planar surface. Peak IQE enhancement by a factor of ~ 1.6 is observed at ~ 1050 nm.

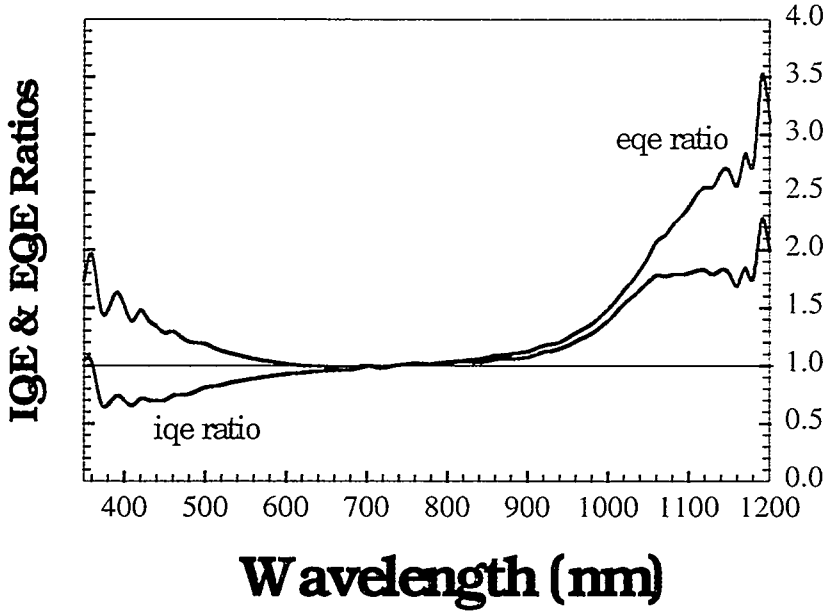

Figure 13. IQE and EQE ratios (texture/planar) of randomly textured surface showing significant improvements in the 900-1200-nm spectral region, no damage removal treatments were done on the cell.

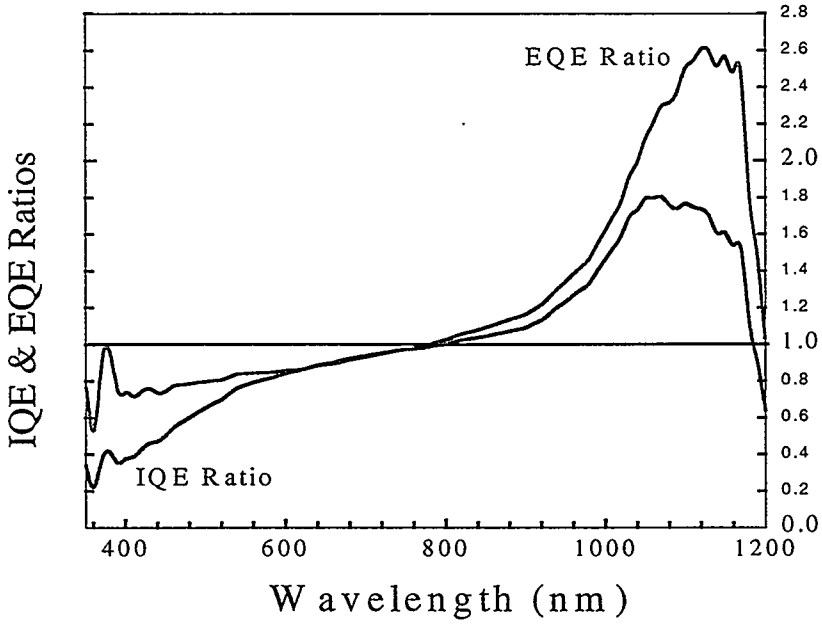

Figure 14. IQE and EQE ratios (texture/planar) of randomly textured surface showing significant improvements in the 900-1200-nm spectral region, 30-sec KOH etching was done to remove some of the surface damage.

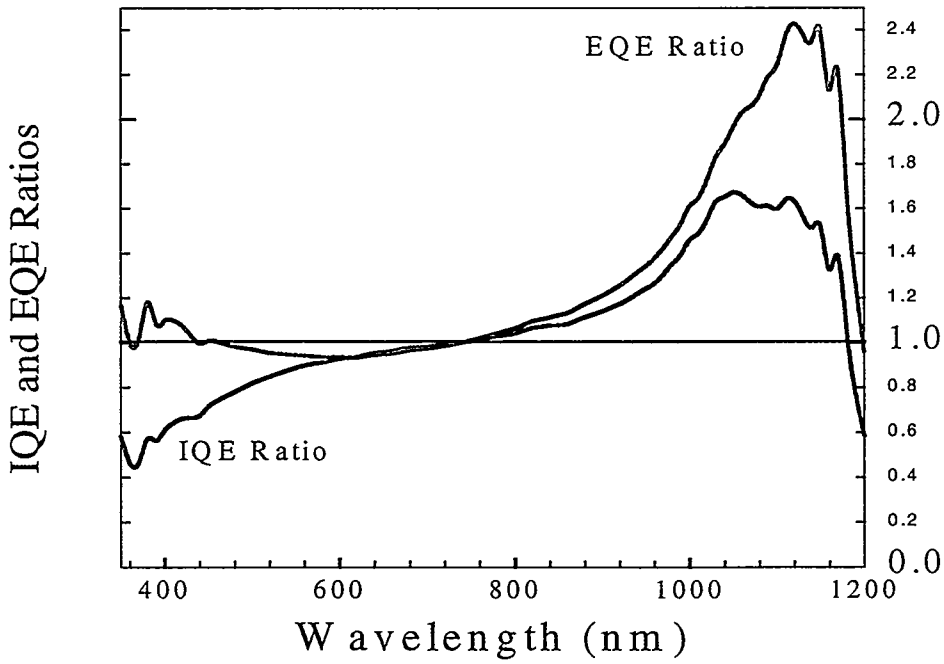

Figure 15. IQE and EQE ratios (texture/planar) of randomly textured surface showing significant improvements in the 900-1200-nm spectral region, 10-sec nitric acid etching was done to remove some of the surface damage.

In summary, surface damaged sustained by RIE texturing process can be removed by wet chemical etching without losing structural-dependent enhancement in the near IR region. For (100) Si, it appears that crystalline-dependent KOH etching does not significantly impact IR response, whereas anisotropic nitric acid etching tends to be less beneficial.

2h. Discussion of Results and Future Work

A useful benchmark of the effectiveness of the RIE texturing with DRE treatments is a comparison of their IQEs with the wet-chemically textured surfaces. Wet-chemically textured surfaces have large features, and have not been subjected to plasma processes, therefore, these surfaces are expected to be well passivated. Figure 16 shows IQE, EQE, and reflectance of both RIE textured and wet-chemically textured solar cells. For the RIE cell, surface damaged layer was removed by 20-sec nitric acid etch. Comparison of IQEs shows that the RIE-textured surface is superior to the chemically textured surface in the short wavelength (~ 350-450 nm) and the long wavelength (~ 750-1200 nm) spectral regions. The wet-chemically textured surface has superior response in most of the visible spectral range (~ 450-750 nm). This is better illustrated in Fig. 16d, which plots the IQE & EQE ratios of the RIE to the chemically textured surfaces. The SWR for the RIE textured surface at ~ 7 % is slightly higher than the wet-chemically textured surface value of ~ 6.3 %. Therefore, the measurements in Fig. 16 demonstrate that the random RIE textured surfaces with appropriate DRE treatments have IQE response comparable to the wet-chemically textured surfaces, and in addition, provide ~ 50 % improvement at ~ 1100-1150-nm spectral region. With further process optimization, this is expected to improve.

The solar cell fabrication process used here has been optimized on random, wet-chemically etched surfaces. For RIE-textured surfaces, feature dimensions are smaller than optical wavelengths, therefore, some optimization will be required. Some of the other related processes that require optimization are listed below.

i. Determination of best texture/damage removal combination,
ii. Determination of optimum p-n junction configuration for nanostructured surfaces,
iii. Statistical analysis of best texturing scheme,
iv. Understanding of RIE processes leading to various textures,
v. Understanding of light interaction with various textures, and
vi. The best texturing process application to mc-Si solar cells.

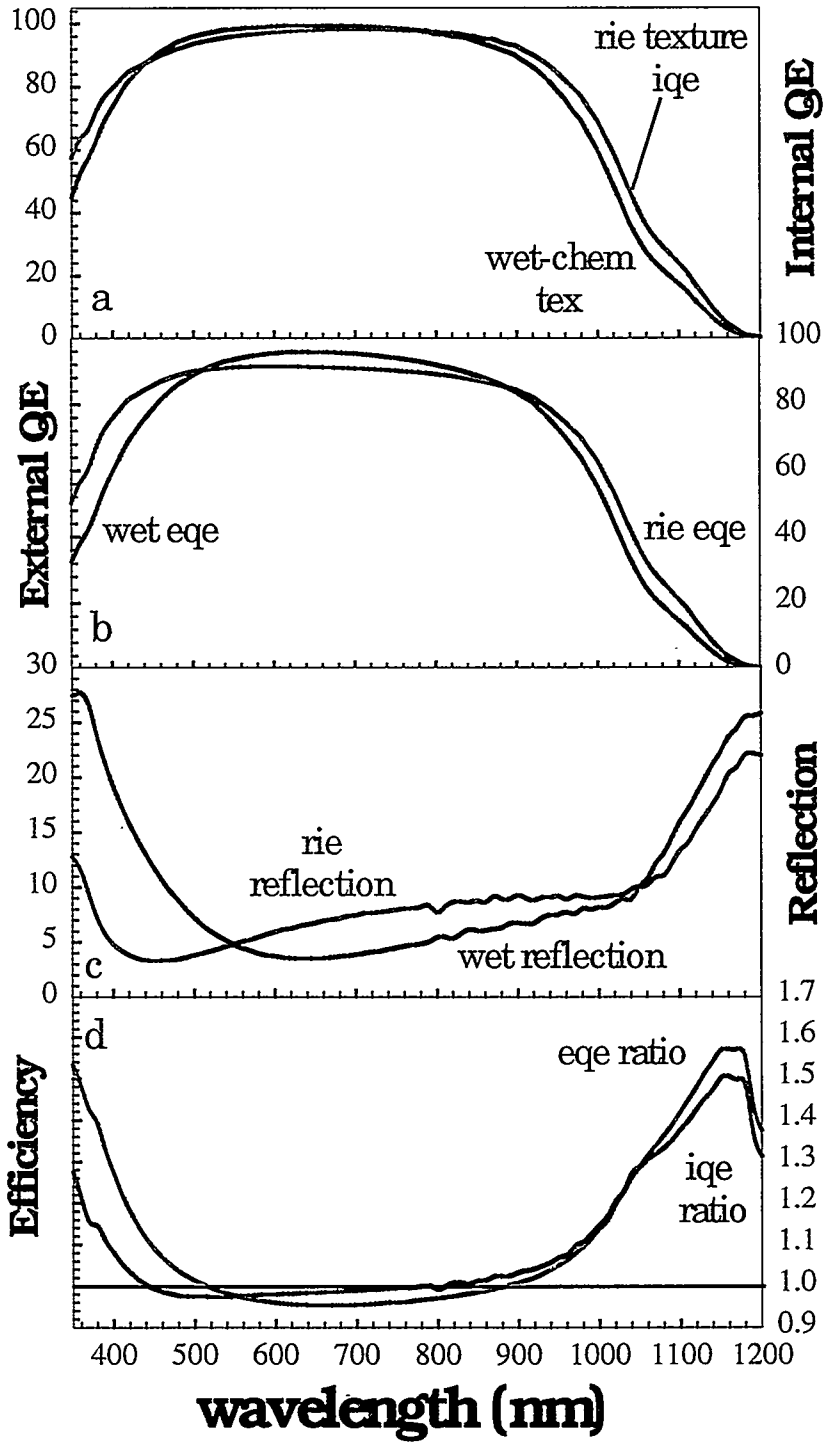

Figure 16. IQE, EQE, and reflectance responses of RIE and wet-chemically textured solar cells, the RIE-textured cell had been wet-chemically etched with nitric acid to remove surface damage.

3. Part II. Nanoscale Periodic Structures for Solar Cell Applications

3a. Sub-wavelength Periodic Structures for Solar Cells

Reducing reflection losses can significantly enhance performance of Si solar cells. Thin-film anti-reflection films are most often used to reduce surface reflection. Another widely used approach is based on wet-chemical etching of (100) Si to form randomly oriented inverted pyramids [3]. This wet-chemical texturing mechanism requires (100) crystal orientation, and can't be applied to multi-crystalline surfaces. Also, the lateral dimensions of the pyramids are a few micrometers, which restricts their applicability to relatively thick substrates. Enhanced light absorption in these types of textures can be understood on the basis of geometrical optics considerations. Basically, all the light outside of a narrow cone defined by the critical angle $\theta_c=\text{asin}(1/n_{Si}) \sim 16°$ is totally internally reflected. Therefore, by re-directing light inside Si at oblique angles ($>\theta_c$), total internal reflection causes multiple bounces within the cell enhancing its absorption probability. In recent years, surface texturing techniques based on random reactive ion etching have been developed [9-14]. Such surfaces also referred to as "black Si" consist of either columnar or triangular profiles varying in linewidths, spacing and depths from ~ 50-500 nm, and typically exhibit broadband low surface reflection for wavelengths < 1 μm of ~ 1-5 %. A primary advantage of RIE texturing is its applicability to single and multi-crystalline surfaces. RIE-textured surfaces are susceptible to the plasma-induced surface damage that substantially reduces internal quantum efficiency in the UV-Visible spectral regions. Nevertheless, large area, RIE-textured mc-Si solar cells with an efficiency of ~ 17.1 % have been reported [15]. Another similar approach aimed at reduced reflection requires anodic etching of Si to form a porous layer at the front surface [16]. Porous Si also supports a wide range of nanoscale features with broadband reflection reduction similar to black Si surfaces. However, the complex chemical and morphological nature of porous Si makes it unsuitable for solar cell applications. Reduced reflection behavior of these subwavelength surfaces can be understood on the basis of physical optics considerations. The nanoscale textures represent a smooth transition, somewhat similar to a graded index film, in refractive index from the incident medium to the bulk Si [24].

Because, the random RIE textured surfaces represent a wide distribution of feature sizes, a more uniform patterning capability is expected to provide improved reflection control. Broadband anti-reflection characteristics of 1D sub-micrometer dielectric [25] and metal grating structures [26] have been reported in literature. Gaylord, et al., [27-28] have developed rigorous theoretical modeling of 1D, rectangular profiled gratings showing zero reflectance for a suitable range of grating parameters. Raguin and Morris [29] have carried out extensive modeling studies of broadband anti-reflection characteristics of 1D triangular and 2D pyramidal profiles. Spectrally selective anti-reflection characteristics of grating structures have also been reported. Sheng et al., [30] have developed rigorous formalism which predicts substantial enhancement in short circuit current for thin-film solar cells in 800-900 nm spectral range. Heine and Morf [31] have demonstrated enhanced absorption in near IR spectral region of thin Si solar cells by shallow grating structures. In this diffractive optics approach, grating parameters are designed to enhance coupling energy into obliquely propagating diffraction orders. This increases the optical path lengths in the Si, which enhances absorption probability particularly near the band edge, where Si absorption is extremely weak. Anti-reflection grating structures have also been employed to improve performance of vertical cavity surface emitting lasers [32]. Strong, polarization-dependent reflection characteristics of 1D a-Si gratings with periods in 50-900 nm range have also been investigated [33].

Here, we report on reflection and internal quantum efficiency (IQE) evaluation of a wide range of 1D and 2D grating structures with periods in 300-1000 nm range. In order to isolate variation in material properties, planar and grating solar cells were formed side-by-side on the same substrate. Surface passivation was achieved by a thin (~ 10 nm) oxide film grown during back surface field formation. The rest of this report is divided into the following sections: section 3b describes the fabrication of sub-μm Si gratings using wet-chemical and plasma etching techniques, section 3c describes hemispherical reflection from 1D and 2D gratings, section 3d presents

IQE measurements from grating solar cells, section 3e discusses the diffraction approach for solar cells, section 3f discusses results, and finally, section 4 contains a short summary.

3b. Etching of Periodic Structures in Si

We have developed low-cost, large-area interferometric lithography (IL) techniques to pattern a wide range of 1D and 2D periodic structures [34]. Interference between two coherent laser beams produces a simple periodic pattern at $d=\lambda/2\sin\theta$, where λ is the exposure wavelength, and 2θ is the angle between the two intersecting laser beams. For λ=355 nm, θ= 60 °, periods down to ~ 200-nm can be easily fabricated. Typically, grating structures are first formed in photoresist followed by pattern transfer to Si using an appropriate combination of wet and dry etching techniques. Figures 17 & 18 show scanning electron microscope pictures of triangular and rectangular profile gratings etched in Si using RIE and wet-chemical etching methods [8]. The triangular structures shown in Fig. 17 are characterized by periods of ~ 670 and 420 nm with full width at half-maximum depths (FWHM) at ~ 300 nm and 100 nm respectively. Grating depths respectively are 800 and 500 nm. These gratings were etched in Si using SF_6/O_2 plasma chemistry [35]. The rectangular profiles shown in Fig. 18 were wet-chemically etched in (110) Si using a 40% KOH solution. Large etch rate variation between <111> and <110> planes gives rise to these high aspect ratio features [23]. The grating periods in this case were 500 nm and 300 nm, with respective linewidths at ~ 130 and 50 nm at ~ 1000 nm depth. Figure 19 shows SEM profiles of two types of 800-nm period 2D RIE etched gratings. The post pattern is characterized by FWHM linewidths ~ 400 nm, and etch depth of ~ 1000 nm. The hole pattern has a FWHM linewidth of ~ 270 nm and etch depth of ~ 800 nm.

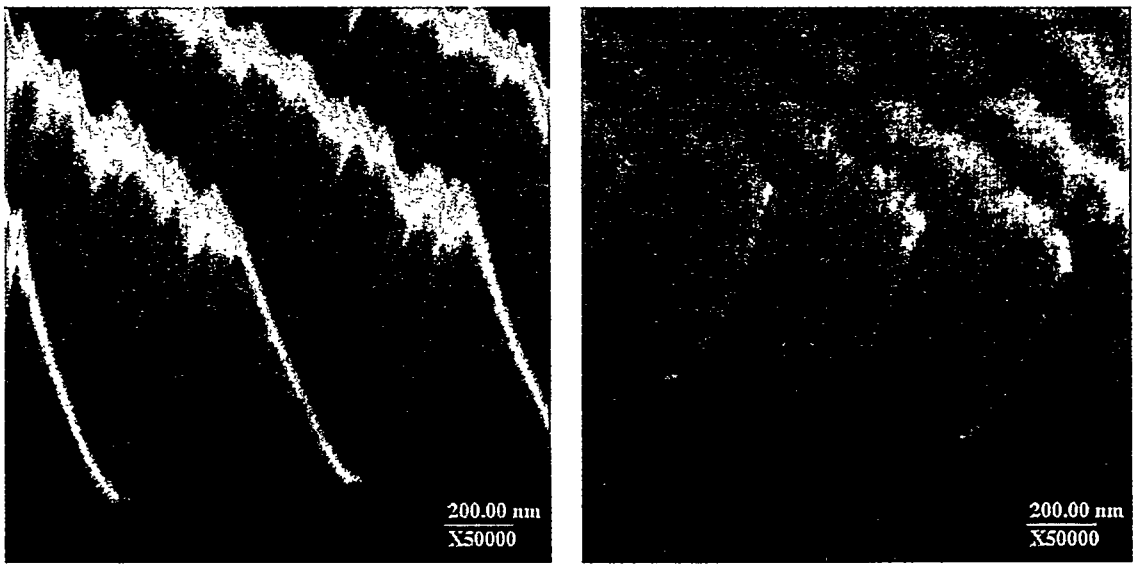

Figure 17. SEM pictures of 670-nm period (left) and 420-nm (right) Si gratings fabricated using RIE.

3c. Hemispherical Reflectance Measurements

Figure 20 shows absolute hemispherical reflectance measurements from triangular gratings shown in Fig. 17. For comparison, reflectance from polished Si, conventionally wet-chemically textured, and the RIE-textured random pyramid surfaces measured under identical conditions are also shown. It is seen that broadband reduced reflection is observed from these grating profiles. For the two grating periods, lower reflection is observed from the finer period structure. For both gratings, overall reflection is lower than that observed from the wet-textured surface. The lowest reflection is seen from the random RIE-textured surface. The typical linewidths of RIE

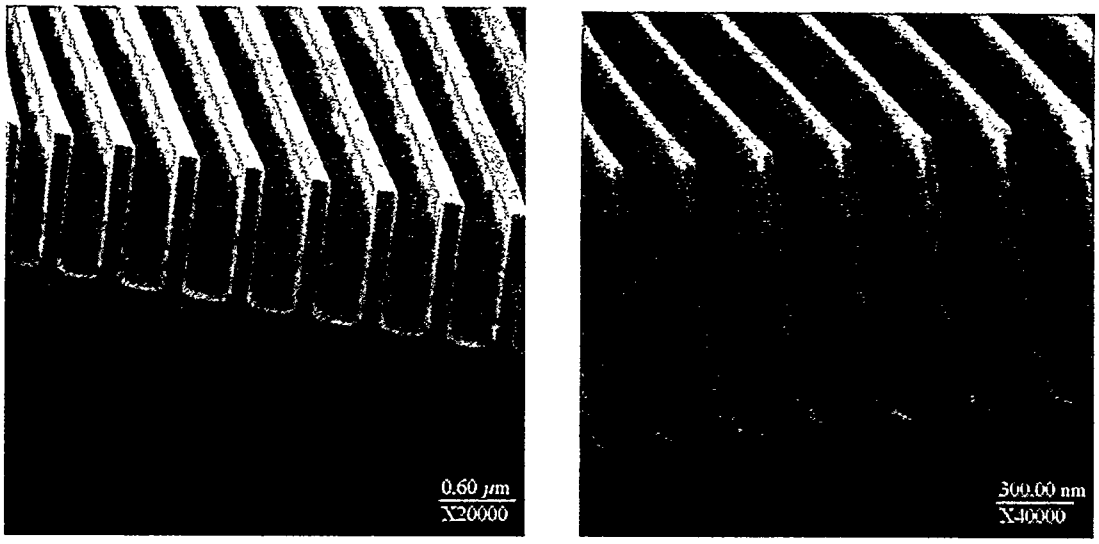

Figure 18. SEM pictures of 500-nm period (left) and 300-nm (right) rectangular profiled Si gratings.

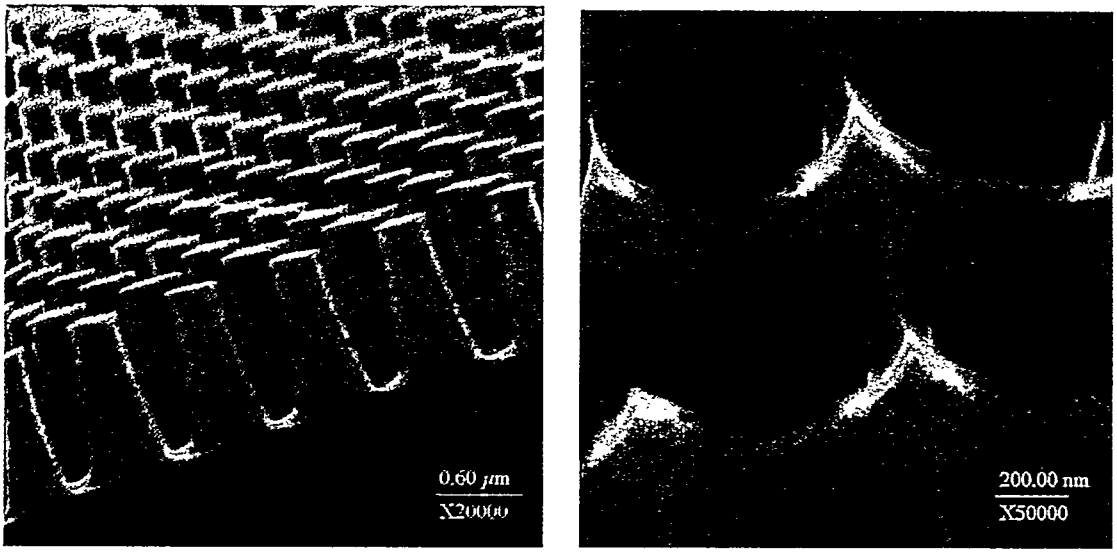

Figure 19. SEM pictures of 800-nm period posts (left) and holes (right) formed in Si using RIE.

textured surfaces (Fig. 17) were in 50-100 nm range, with similar spacing, and etch depths. Comparison of FWHM linewidths in Figs. 2 & 17 suggests that reflection is a strong function of linewidth and its slope, with lower reflection resulting from smaller linewidths.

Hemispherical reflectance measurements of rectangular profiled gratings are shown in Fig. 21. Here, we observe a number of narrow, low reflectance spectral bands. For the 500-nm period structure, lowest reflection is observed at $\lambda \approx 500$ nm, while the rest of the spectral bands are not as pronounced. For the 300-nm period grating, lowest reflection is seen at $\lambda \approx 320$ nm. For this grating, overall reflection increases as a function of wavelength. We notice that in the short wavelength regime, reflection reduction appears to be a function of linewidth, gratings with smallest linewidths exhibit lowest reflection. However, as opposed to the broadband low reflection of the random RIE surfaces, a more uniform 50-nm linewidth grating structure exhibits a continuous reflection increase as a function of wavelength. The hemispherical measurements shown in Figs. 20 & 21 do not take into account the polarization of incident light relative to grating lines. We have investigated the polarization-dependent normal

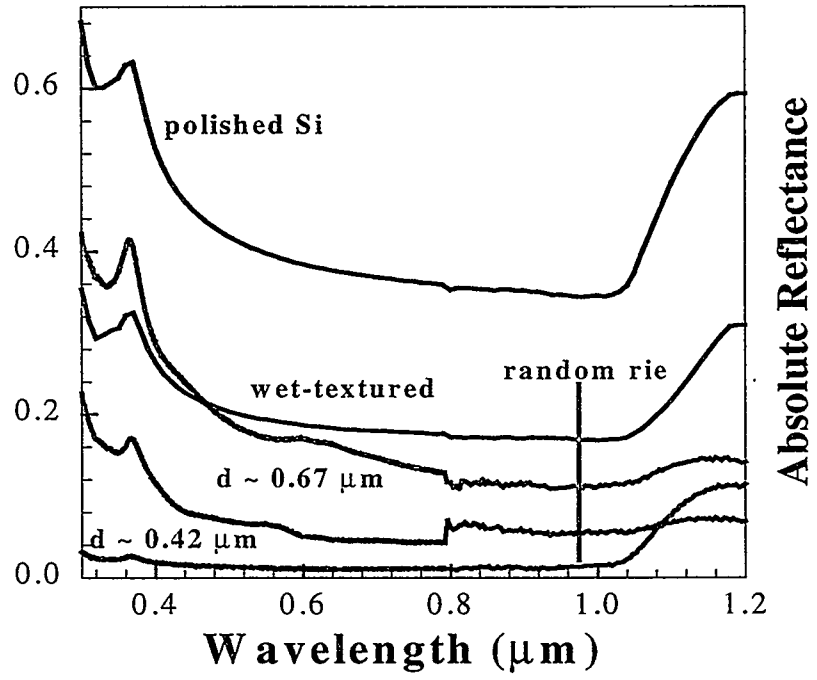

Figure 20. Hemispherical reflectance measurements from triangular profiled, 1D gratings shown in Fig. 17.

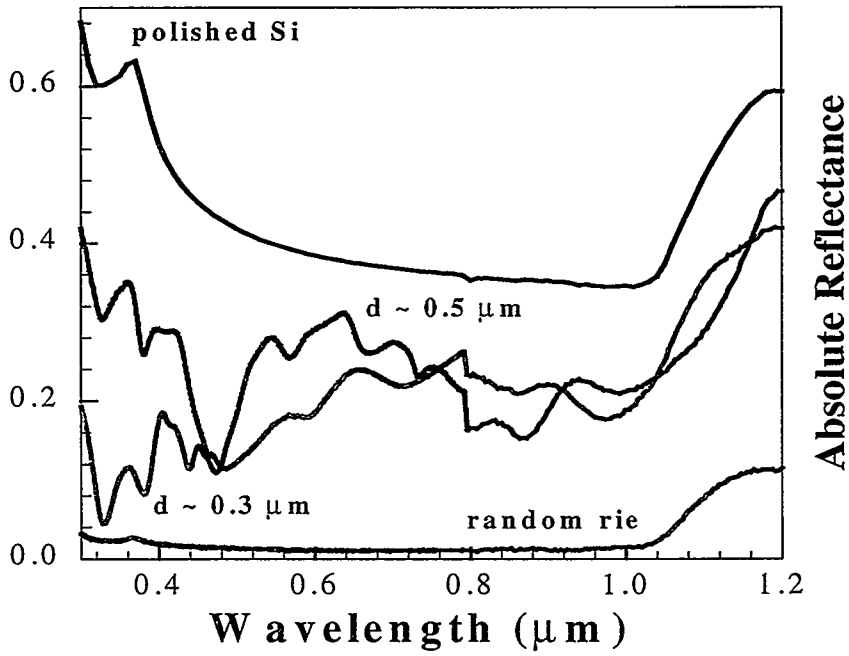

Figure 21. Hemispherical reflectance measurements from rectangular profiled, 1D gratings shown in Fig. 18.

incidence reflection from the 500-nm period grating shown in Fig. 18 (left). Figure 22 shows the normalized reflectance measurements for TE (electric field parallel to grating lines) and TM (electric field perpendicular to grating lines) polarization of incident light. A highly form birefringent behavior is observed. For the TM polarization, a broadband low-reflectance behavior is observed. For TE polarization, narrow low-reflectance spectral bands at ~ 540 nm, 680 nm, and 780 nm are observed. Notice that for the 500-nm period, energy lost in reflection is not coupled into radiative diffraction orders for $\lambda > 500$ nm. Therefore, the energy lost in reflection is redistributed into various transmitted orders. For the 2D structures shown in Fig. 19, polarization effects don't play a significant role. Figure 23 shows the hemispherical reflectance from both the post and hole patterns. For these structures, broadband reduced reflection is observed. The post pattern has a substantially higher overall reflection than hole pattern. For this particular hole pattern, lowest reflection is observed in the near IR region, where it almost matches the random RIE surface.

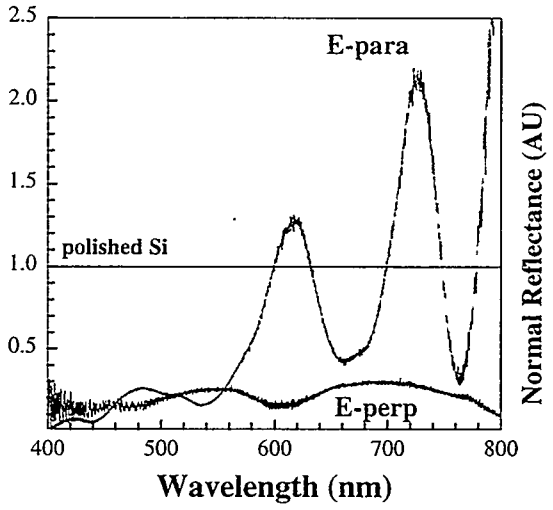

Figure 22. Normal incidence reflection measurements from 500-nm period grating shown in Fig. 18 (left).

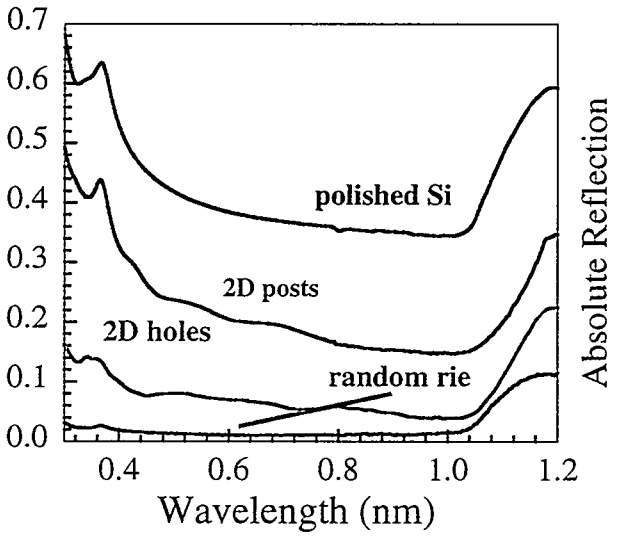

Figure 23. Hemispherical reflectance measurements 2D grating structures shown in Fig. 19.

3d. Internal Quantum Efficiency Measurements of Grating Solar Cells

Figure 24 shows IQE measurements from the planar and 800-nm period 1D grating regions of the same solar cell device. The profile of the grating was similar to that shown in Fig. 17 (left). It is seen that even though the reflection has been substantially reduced, there is no enhancement in IQE mainly due to substantial losses in the 300-900 nm spectral region. This suggests that grating structure promotes absorption close to the surface. A significant fraction of these photo-generated EHPs is lost to recombination due to the RIE-induced surface damage. For the rectangular profiled gratings, we expect to see narrow spectral bands of low reflectance. Figure 25 shows IQE measurements from such a grating structure, measurements from the planar region have also been plotted for comparison. For this 500-nm period grating, reflectance shows resonances at 440 nm, 500 nm, and 680-nm. The grating IQE measurement shows somewhat similar behavior. Notice that these measurements are not completely accurate because of the polarization-dependence of grating reflection, which has not been taken into account during hemispherical reflectance measurements. More precise measurements will result from well-defined polarization of the incident light relative to the grating orientation. Figure 26 shows IQE measurements from the 2D hole pattern shown in Fig. 19 (right). Here, we notice that IQE has been reduced in the 300-800 nm spectral region probably due to the RIE-induced surface damage. A substantial enhancement is observed in the 800-1200-nm spectral region. For this 2D hole pattern, the enhancement in IQE is by as much as a factor of 2.0 over the planar surface, and peaks at $\lambda \approx 1.1$ μm.

From the IQE measurements of relatively deep, high aspect ratio grating solar cells, we can draw some conclusions.

a) Grating reflection can be substantially reduced either in narrow, or broad spectral regions,
b) RIE-induced surface damage significantly degrades short-wavelength response of grating cells, and
c) Appropriately designed 2D grating patterns can lead to significant IQE enhancements in the near IR spectral region.

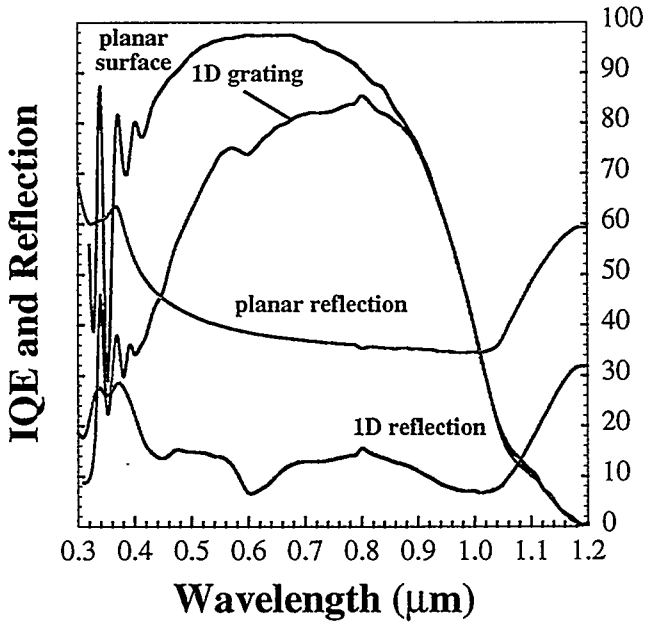

Figure 24. IQE and reflectance measurements from planar and 1D grating solar cells.

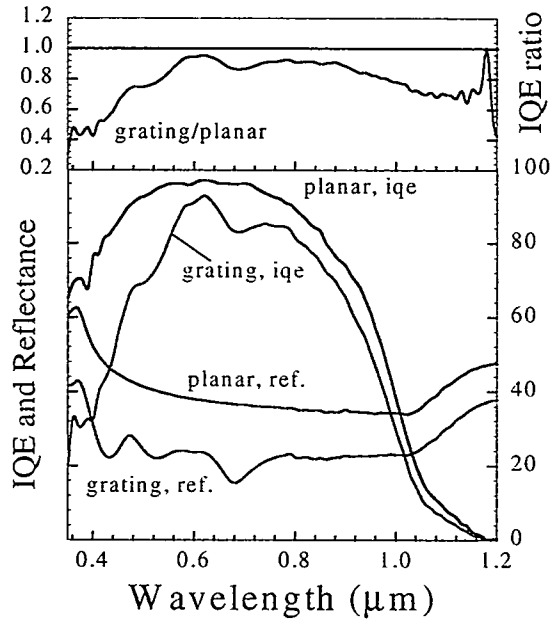

Figure 25. IQE and reflectance measurements from planar and 500-nm period, 1D grating solar cells.

It should be stressed again that grating solar cell fabrication process has not yet been optimized. The fabrication process followed had been optimized on large (~ few micrometers) textured surfaces. For grating solar cells, surface junctions would need to be further optimized, i.e., a conformal junction around each grating line is expected to substantially reduce recombination losses. RIE-induced surface damage can be reduced by various surface passivation treatments such as annealing, thermal oxidation, and wet-chemical etches discussed earlier.

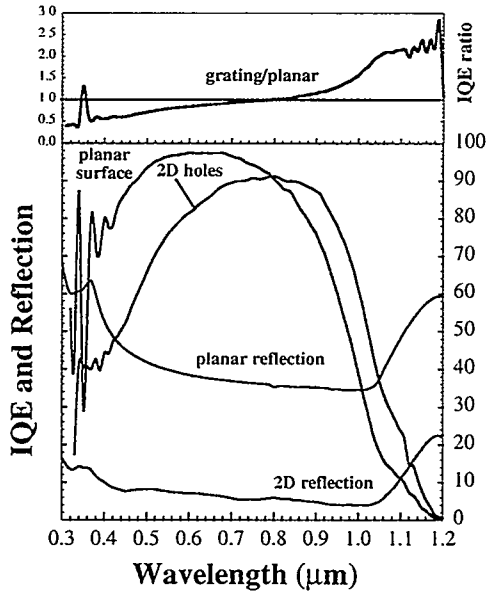

Figure 26. IQE and reflectance measurements from planar and 800-nm period, 2D grating solar cells.

3e. Diffractive Approach for Solar Cells

The gratings discussed above served primarily as anti-reflection surfaces. However, RIE-induced surface damage degrades cell performance in the short wavelength region. An alternative approach for enhanced optical coupling in to Si surface has been investigated. This approach is similar to the diffractive optics developed earlier by Heine and Morf [31] for thin film solar cells. In diffraction approach, enhanced IR absorption inside Si is achieved by efficient coupling to diffraction orders inside Si. Figure 27 shows an experimental manifestation of this concept. The grating etched at the front surface is characterized by its period d, linewidth l, and depth h. For light incident normally, the grating period is chosen such that there are no radiative diffraction orders in air. Due to high index of Si, there a number of propagating diffraction orders inside Si. Here, a symmetric profile is shown, which results in equal energy coupling into the ±1 and ±2-diffraction orders propagating at angles θ_1 and θ_2 respectively. For a conventional grating structure, higher orders normally carry less energy, however, grating structures can be designed for maximum coupling into any transmitted diffraction order. In comparison with normally propagating zero order, optical path lengths of first and second diffraction orders are increased by $1/\cos\theta_1$ and $1/\cos\theta_2$ respectively. In Fig. 28, we have plotted the angular variations of these diffraction orders inside Si for 500 and 300-nm periods. We notice that for a fixed period, diffraction order angles increase as a function of wavelength until it approaches ~ 90 °, beyond which it becomes evanescent. For the 500-nm period grating, the first diffraction order is always propagating with a maximum angle of ~ 42 ° at λ=1.2 μm, the second diffraction order becomes evanescent at λ ~ 0.9 μm. For the 300-nm period grating, the first diffraction order becomes evanescent at λ ~ 0.96 μm, while the second order becomes evanescent at λ ~ 0.6 μm. Therefore, enhanced absorption particularly in the near IR region, and close to the surface can achieved by designing a grating structure which couples maximum energy into either first, or second diffraction orders propagating at large (> 60°) angles. We have done preliminary numerical modeling using commercially available software GSOLVER™. The model calculations for triangular and rectangular profiles indicate that for propagation angles

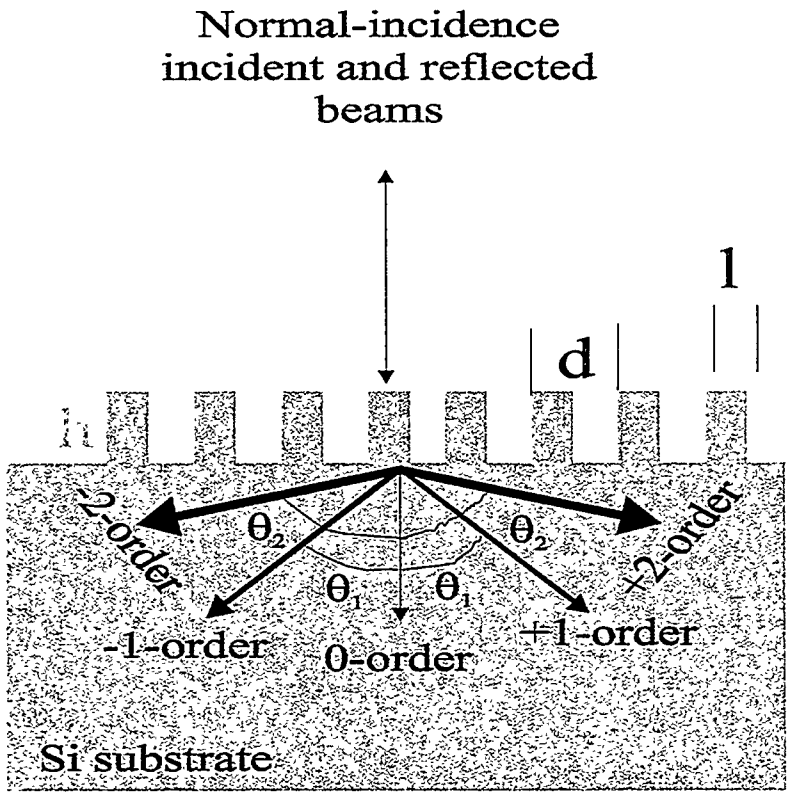

Figure 27. Oblique coupling into Si using a diffraction grating.

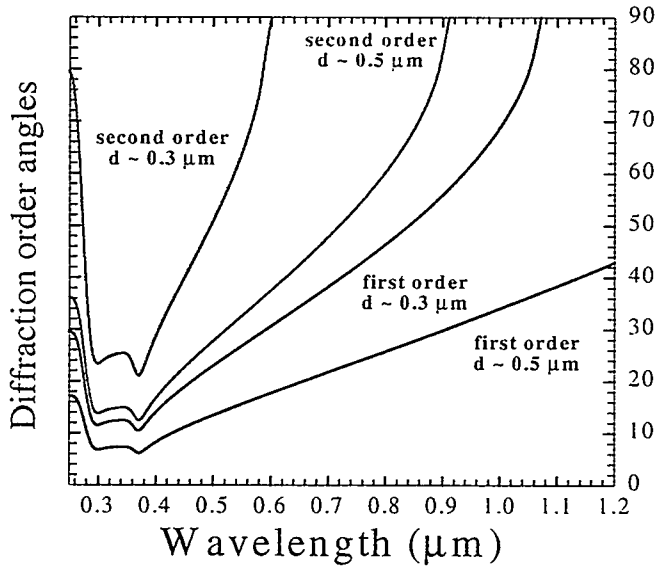

Figure 28. Angular variation of diffraction orders as a function of wavelength.

beyond 70 °, the coupling into diffraction orders is reduced sharply. With blazed and more complex profiles [36], it may be possible to couple maximum energy into diffraction orders propagating at angles in 70-90° range. The model calculations also demonstrate the almost periodic dependence of coupling efficiency on grating depth. Figure 29 shows an example of such calculation for the transmitted zero order and the first diffraction order for a 50 % duty cycle, 400-nm period grating incident normally with TE-polarization at λ=1.0 μm. This calculation shows that maximum efficiency in the first order is achievable at depths of ~ 0.2-0.3 μm and 0.7 μm due to energy coupling out of the reflection and transmission zero orders.

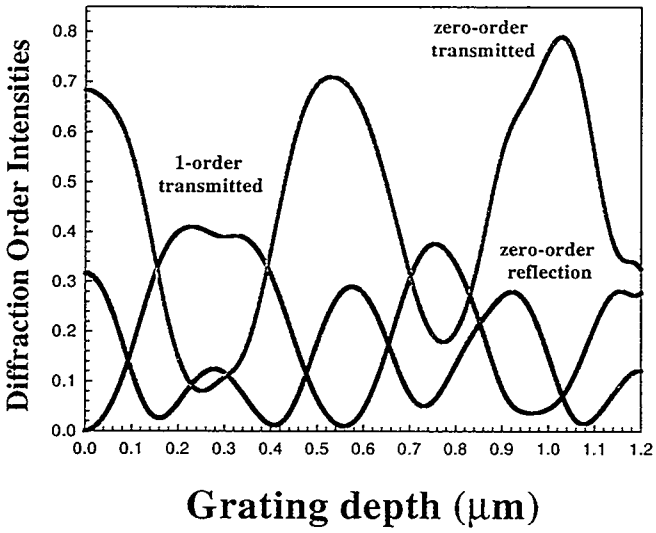

Figure 29. Calculated diffraction efficiency variation as a function of grating depth.

In order to test the validity of the diffraction approach, we investigated 1D and 2D grating solar cells with depths ~ 0.2-0.25 μm. Figure 30 shows IQE measurements from a 500-nm period, 2D grating structure. It is seen that IQE is still reduced in the short wavelength region, although significantly less than for the deeper 2D grating shown in Fig. 19. Also, the hemispherical reflection shows a broadband reduction. The IQE from the grating structure is enhanced in ~ 800-1200-nm spectral region. The ratio of IQEs also plotted in Fig. 30 shows near IR (~ 1.05-1.2 μm) improvement by a factor of 2.1 relative to the planar surface. Figure 31 shows similar measurements from the 300-nm period, 2D structure. Here also, IQE is degraded in the 350-700-nm spectral region, however, enhancement is observed in the long wavelength region, with a maximum enhancement of ~ 1.75 at $\lambda \sim 1.1$ μm.

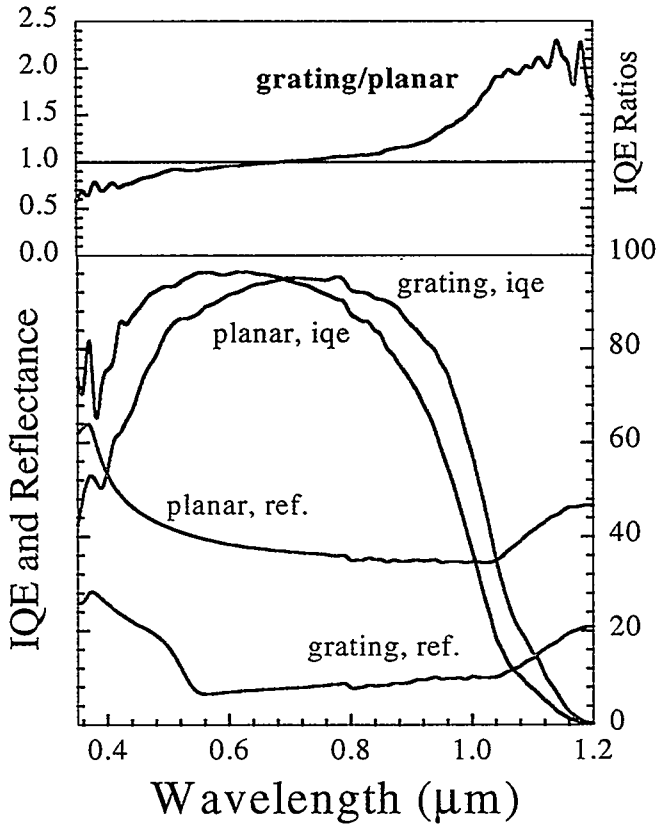

Figure 30. IQE and reflectance measurements from planar and 2D, 500-nm period grating solar cells.

3f. Discussion of Results

We have evaluated IQE response of a number of 1D & 2D grating solar cells. Our measurements show that grating structures can be designed either for broadband, or narrow band anti-reflection behavior. For a broadband absorptive surface such as that shown in Fig. 17, the IQE response (Fig. 24) is severely degraded due to RIE-induced surface damage. From the lack of enhancement in the long wavelength region, it can be concluded that the triangular-profiled grating structures act as a graded index film with most of the energy coupled into the transmitted zero order inside Si. Practical utility of this type of grating profile is critically dependent on the degree of surface damage incurred during reactive ion etching. Improved cleaning and damage removal etches discussed earlier can remove some of the surface damage. Much more significant improvement can be achieved by replacing the RIE etching with wet-chemical etching to form triangular profiles, which predict comparable coupling efficiencies in the transmitted diffraction orders [7].

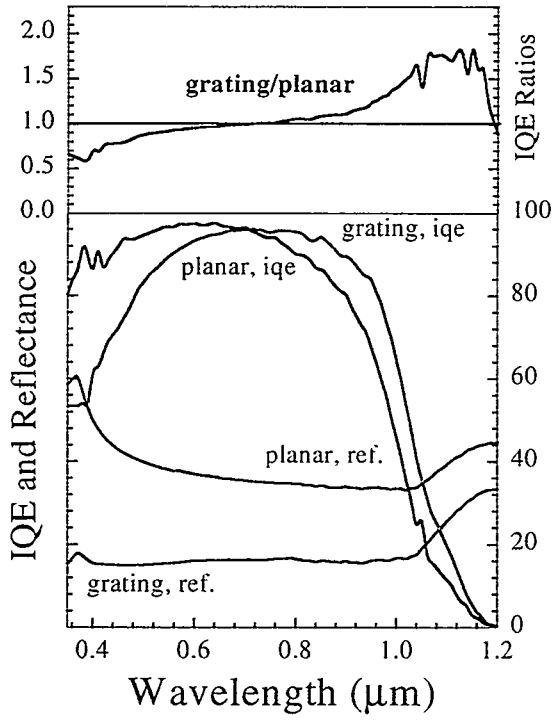

Figure 31. IQE and reflectance measurements from planar and 2D, 300-nm period grating solar cells.

A key aspect of grating structures is the enhancement in the long wavelength response. The 2D hole pattern shown in Fig. 19 (right) is good example of this behavior. This particular structure not only exhibits broad band low hemispherical reflectance, but also creates significant IQE enhancement in 800-1200-nm spectral region. Similar, although not as pronounced, response has been observed from 500-nm and 300-nm period structures. These type of grating structures do not behave as graded index anti-reflection films, rather they act as a diffractive texture that couples significant energy into transmitted diffraction orders inside the Si. A rigorous modeling of 2D patterns is required in order to understand the behavior of such structures.

Anti-reflection films reduce surface reflection. We have investigated reflection and IQE response of grating structures following deposition of anti-reflection nitride films. Figure 32 shows IQE and reflectance measurements from a polished Si surface following nitride film deposition. A comparison of surface reflection before and after nitride disposition illustrates significant reflection reduction from the anti-reflection nitride film. The IQE comparison shows comparable long wavelength response, however, slightly lower short wavelength response is obtained following the nitride deposition. This is probably due to surface contamination as there was significant time lag between these two measurements. Figure 33 shows IQE and reflectance measurements from a 1D rectangular-profiled grating following nitride film deposition, for comparison reflectance and IQE responses without nitride film have also been plotted. We notice that deposition of nitride film has eliminated narrow-band reflectance behavior. Instead, surface reflectance is significantly reduced over a broad spectral region. Also, the IQE response shows no spectral structure. Figure 34 shows IQE and reflectance measurements from the 800-nm period 2D hole pattern following the nitride film deposition, for comparison reflectance and IQE responses without nitride film have also been plotted. We notice that deposition of nitride film has slightly lowered the reflectance in 350-900-nm spectral region. In 900-1200-nm spectral region, hemispherical reflectance remains unchanged, although there is slight increase in reflection at ~ 1200 nm. The IQE responses before and after nitride film deposition are also comparable with slight degradation observed in the short wavelength region. The ratio of

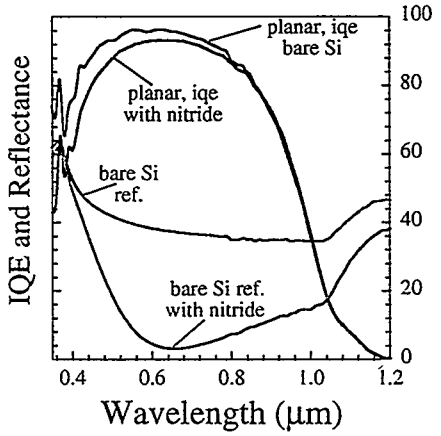

Figure 32. IQE and reflectance measurements from planar solar cells before and after AR nitride film.

IQE from grating-to-planar regions with the nitride deposition shows a behavior identical to that without the nitride film. This suggests that the anti-reflection films can further reduce grating reflectance without sacrificing the long wavelength enhancement in IQE. Figure 35 shows IQE and reflectance measurements from the 500-nm period 2D grating structure following the nitride film deposition, for comparison reflectance and IQE responses without nitride film have also been plotted. We notice that deposition of nitride film has slightly lowered the reflectance in 350-450-nm spectral region. In 550-1050-nm spectral region, hemispherical reflectance remains unchanged, although there is slight increase in reflection at ~ 1050-1200-nm spectral region. The IQE responses before and after nitride film deposition are also comparable with slight degradation observed in the entire spectral region. The ratio of IQE from grating-to-planar regions with the nitride deposition shows a behavior identical to that without the nitride film, and matches the behavior of 2D-hole pattern. Finally, Fig. 36 shows IQE and reflectance measurements from the 300-nm period 2D grating following the nitride film deposition, for comparison reflectance and IQE responses without nitride film have also been plotted. We notice that deposition of nitride film has significantly lowered the reflectance over the entire spectral region. The IQE responses before and after nitride film deposition are also comparable with slight degradation observed in the UV-Visible wavelength region. The ratio of IQE from grating-to-planar regions with the nitride deposition shows a behavior identical to that without the nitride film, and matches that of the 2D-hole pattern.

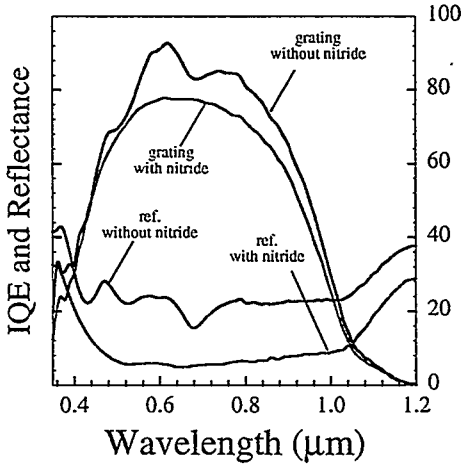

Figure 33. IQE and reflectance measurements from 1D rectangular grating cell before and after AR nitride film.

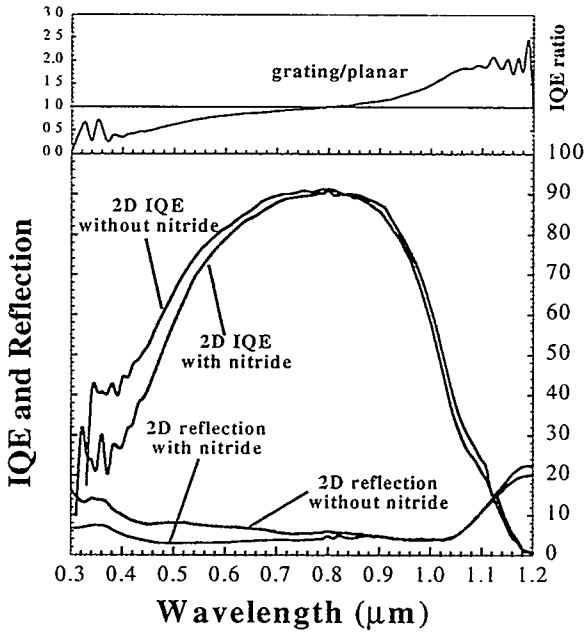

Figure 34. IQE and reflectance measurements from 2D hole-pattern cell before and after AR nitride film.

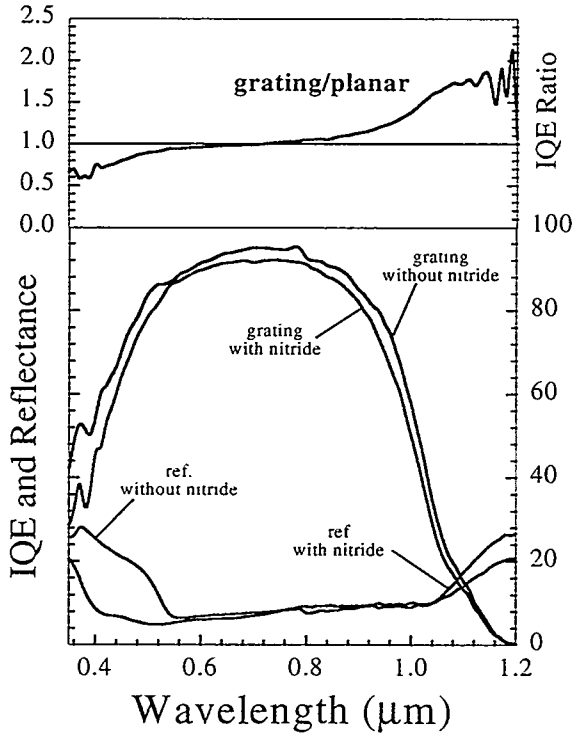

Figure 35. IQE and reflectance measurements from 2D, 500-nm period solar cell before and after AR nitride film.

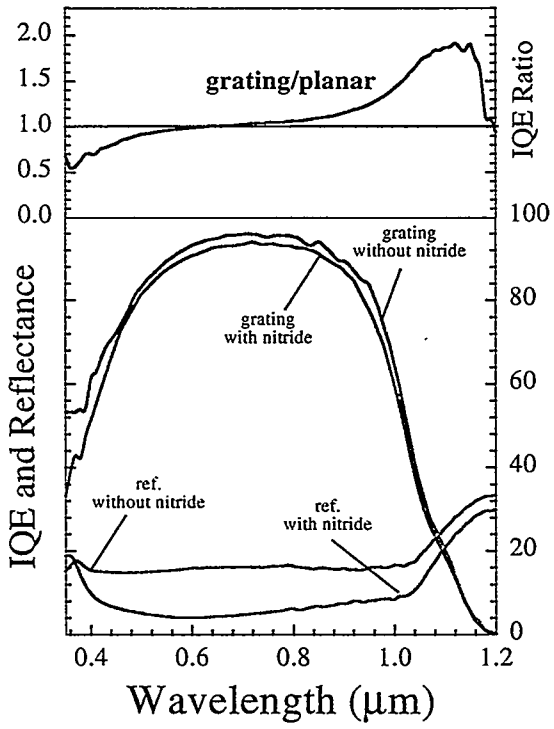

Figure 36. IQE and reflectance measurements from 2D, 300-nm period solar cell before and after AR nitride film.

4. Summary

We have presented a detailed reflectance and IQE characterization of nanostructured Si surfaces. Nanoscale surfaces formed by using either random or periodic RIE texturing techniques. RIE textured surfaces are susceptible to surface contamination, and plasma-induced surface damage, which can severely degrade their IQE response. By combining wafer cleaning with wet-chemical damage removal etches, an undamaged Si surface can be recovered without significant reflection losses. This is supported by a comparison of IQEs of random wet-chemically textured and DRE treated RIE-textured solar cells. An interesting feature of the RIE-textured surfaces is their superior response in the long wavelength region. This enhancement could be attributed to the scattering of light into obliquely propagating transmitted diffraction orders inside the Si substrate. The random RIE texturing techniques are ideal candidates for multicrystalline Si solar cells, where no other texture-assisted light trapping schemes are readily available.

From an evaluation of various periodic structures, three trends can be distinguished. Broadband, polarization-independent, low reflective behavior of 1D triangular profiles appears identical to the graded-index anti-reflection thin films. IQE response of such surfaces provides no significant enhancement in any particular spectral region, instead UV response is severely degraded due to the RIE-induced surface damage. Rectangular-profiled, 1D grating structures exhibit absorption in narrow spectral bands, somewhat similar behavior is observed in their IQE response. The most interesting behavior is seen for the third type of grating structure that combines the broadband anti-reflection behavior with significant IQE enhancement in the long wavelength region. The long wavelength IQE response for these grating structures is similar to the random, RIE-textured solar cells. With appropriate surface passivation of grating surfaces, this enhancement is expected to be significantly larger than the randomly textured surfaces.

In summary, the nanostructured Si surfaces with adequate surface passivation can provide significant performance enhancement of solar cells. Random, RIE-texturing techniques are an obvious candidate for large area, low-cost texturing of mc-Si solar cells. With appropriate surface passivation, grating-texturing techniques can potentially outperform the randomly textured surfaces. Grating-texturing techniques are expected to find applications in the thin-film and space solar cells, for both of which enhanced IR response is required either due to lack of sufficient film thickness for absorption, or the radiation-induced surface and bulk damage.

5. References

1. *Fundamental of Solar Cells*, A. L. Fahrenbruch and R. H. Bube, Academic Press (1983).
2. *Solar cells and Semimetals, Vol. II*, edited by H. J. Hovel, Academic Press (1975).
3. P. Campbell and M. A. Green, Appl. Phys. Lett. **62**, 243 (1987).
4. J. M. Gee, IEEE PVSC-**12**, 549 (1988).
5. E. Yablonovitch, Jour. Opt. Soc. Amer. **72**, 899 (1982).
6. H. W. Deckman, C. R. Wronski, H. Witzke, and E. Yablonovitch, Appl. Phys. Lett. **42**, 968 (1983).
7. S. Kemme, Saleem H. Zaidi, and J. M. Gee, Submicron Diffractive Gratings for Thin Film Solar Cell Applications, Presented at the **9th** Workshop on Crystalline-Silicon Materials and Processes, Breckenridge, August 1999.
8. Saleem H. Zaidi, An-Shyang Chu, and S. R. J. Brueck, J. Appl. Phys. **80**, 6997 (1996).
9. J. I. Gittleman, E. K. Sichel, H. W. Lehman, and R. Widmer, Appl. Phys. Lett. **35**, 742 (1979).
10. H. G. Craighead, R. E. Howard, and D. M. tenant, Appl. Phys. Lett. **37**, 653 (1980).
11. H. G. Craighead, R. E. Howard, J.E. Sweeney, and D. M. Tenant, J. Vac. Sci. Technol. **20**, 316 (1982).
12. H. G. Craighead, R. E. Howard, and D. M. Tenant, Appl. Phys. Lett. **38**, 74 (1981).
13. H. Jansen, M. de Boer, R. Lichtenberg, and M. Elwenspoek, J. Micromech. Microeng. **5**, 115 (1995).
14. A. R. Burgers, C. J. J. Tool, J. D. Hylton, A. W. Weeber, A. G. B. J. Verholen, J. G. E. Gardeniers, M. J. de Boer, and M. C. Elwenspoek, **2nd** World Conf. On PV conversion, 1531 (1998).
15. Y. Inomata, K. Fukui, K. Shirasawa, **9th** Internat PVSEC, 109 (1996).
16. Y. S. Tsuo, Y Xiao, M. J. Heben, X. Wu, F. J. Pern, and S. K. Deb, PVSC-**93**, 287 (1993).
17. S. W. Pang, D. D. Rathman, D. J. Silversmith, R. W. Mountain, and P. D. DeGraff, J. Appl. Phys. **54**, 3272 (1983).
18. N. Yabumoto, M. Oshima, O. Michikani, and S. Yoshi, Jpn. J. Appl. Phys. **20**, 893 (1981).
19. G. S. Oehrlein and Y. H. Lee, J. Vac. Sci. Technol. **A 5**, 1585 (1987).
20. H. H. Park, H. H. Kwon, J. L. Lee, K. S. Suh, O. J. Kwon, K. I. Cho, and S. C. Park, J. Appl. Phys. **76**, 4596 (1994).
21. H. H. Kwon, H. H. Park, K. S. Kim, C-III Kim, and Y. K. Sung, Jpn. J. Appl. Phys. **35**, Pt 1, 1611 (1996).
22. S. Schafer and R. Ludemann, J. Vac. Sci. Technol. **A 17**, 749 (1999).
23. K. E. Bean, IEEE Trans. Elect. Dev., **ED-25**, 1185 (1978).
24. William H. Southwell, J. Opt. Soc. Amer. **A 8**, 549 (1991).
25. R. C. Enger and S. K. Case, Appl. Opt. **22**, 3320 (1983).
26. Saleem H. Zaidi, M. Yousaf, and S. R. J. Brueck, Jour. Opt. Soc. Amer. **B 8**, 772 (1991).
27. T. K. Gaylord, W. E. Baird, and M. G. Moharam, Appl. Opt. **25**, 4562 (1986).
28. T. K. Gaylord, E. N. Glytsis, and M. G. Moharam, Appl. Opt. **26**, 3123 (1986).
29. D. H. Raguin and G. M. Morris, Appl. Opt. 32, 1154 (1993).
30. Ping Sheng, A. N. Bloch, and R. S. Stepleman, Appl. Phys. Lett. **43**, 579 (1983).
31. C. Heine and R. H. Morf, Appl. Opt. 34, 2476 (1995).
32. J. R. Wendt, G. A. Vawter, R. E. Smith, and M. E. Warren, J. Vac. Sci. Technol. **B 14**, 4096 (1996).
33. L. Zhuang, S. Schablitsky, R. C. Shi, and S. Y. Chou, J. Vac. Sci. Technol. **B 14**, 4055 (1996).
34. Saleem H. Zaidi and S. R. J. Brueck, Jour. Vac. Sci. Technol. **B 11**, 458 (1993).
35. Saleem H. Zaidi and S. R. J. Brueck, IEEE **26th** PVSC, 171 (1997)
36. G. Giaconia, R. Torrini, S. K. Murad, and C. D. Wilkinson, J. Vac. Sci. Technol. **B 16**, 3903 (1998).

DISTRIBUTION

Keith Matthei
GT Solar Technologies
472 Amherst Street
Nashua, NH 03063

Ed Henderson
Matrix Solar
P. O. Box 14740
Albuquerque, NM 87191-4740

Mike Nowland
Spire Corporation
One Patriots Park
Bedford, MA 01810

Steve Hogan
Spire Corporation
One Patriots Park
Bedford, MA 01810

Dr. Juris Kalejs
ASE Americas, Inc.
Four Suburban Park
Billerica, MA 01821-3980

Dr. Mark Rosenblum
ASE Americas, Inc.
Four Suburban Park
Billerica, MA 01821-3980

Dr. James Rand
AstroPower
Solar Park
Newark, DE 19716-2000

Dr. Chandra Khattak
Crystal Systems
27 Congress Street
Salem, MA 01970

Dr. Mohan Narayanan
Solarex Corporation
630 Solarex Court
Frederick, MD 21701

Dr. John Wohlgemuth
Solarex Corporation
630 Solarex Court
Frederick, MD 21701

Mr. Ted Ciszek
National Renewable Energy Lab
1617 Cole Blvd.
Golden, CO 80401-3393

Dr. Bhushan Sopori
National Renewable Energy Lab
1617 Cole Blvd.
Golden, CO 80401-3393

Dr. Jack Hanoka
Evergreen Solar, Inc.
211 Second Avenue
Waltham, MA 02154

Dr. Andrew Gabor
Evergreen Solar, Inc.
211 Second Avenue
Waltham, MA 02154

Ms. Theresa Jester
Siemens Solar Industries
P. O. Box 6032
Camarillo, CA 93011

Dr. Dan Meier
Ebara Solar, Inc.
811 Route 51 South
Large, PA 15025

Prof. Ajeet Rohatgi
Georgia Institute of Technology
777 Atlantic Drive
School of Electrical Engineering
Atlanta, GA 30332

Dr. Jeffrey Mazer
U.S. Department of Energy
Forrestal Bldg., EE-11
1000 Independence Ave., SW
Washington, DC 20585

Dr. Richard King
U.S. Department of Energy
Forrestal Bldg., EE-11
1000 Independence Ave., SW
Washington, DC 20585

Dr. Richard Swanson
SunPower Corporation
430 Indio Way
Sunnyvale, CA 94086

Pierre Verlinden
SunPower Corporation
430 Indio Way
Sunnyvale, CA 94086

Saleem Zaidi
Gratings, Inc.
7104 Jefferson N.E.
Albuquerque, NM 87109

Hong Hou
EMCORE Photovoltaics
10420 Research Rd. S.E.
Albuquerque, NM 87123

Dr. Richard King
Spectrolab, Inc.
12500 Gladstone Avenue
Sylmar, CA 91342-5373

Mr. Frank Ho
Tecstar, Inc.
15251 E. Don Julian Road
City of Industry, CA 91745

Gary Stevens
Matrix Solar
7500 Meridian Place
Albuquerque, NM 87121

0752	Dan Aiken, 6219
0752	David King, 6219
0752	Doug Ruby, 6219
0752	James Gee, 6219
0753	Chris Cameron, 6218
0753	PV Library (5 copies)
0899	Technical Library (2 copies)
0619	RA Desk for DOE/OSTI
9018	Central Technical Files